Comparison of SARS-CoV-2 variants in primary human nasal cultures indicates Delta as most cytopathic and Omicron as fastest replicating

Nikhila S Tanneti[1], Anant K Patel[1], Li Hui Tan[2], Andrew D Marques[1], Ranawaka A.P.M. Perera[1], Scott Sherrill-Mix[1,6], Brendan J Kelly[3], Ronald G Collman[3], Kyle Rodino[3], Carole Lee[1], Frederic D Bushman[1], Noam A Cohen[2,4,5], Susan R Weiss[1,*]

[1]Department of Microbiology, [2]Department of Otorhinolaryngology- Head and Neck Surgery, [3]Department of Medicine, Perelman School of Medicine, University of Pennsylvania, Philadelphia, USA.

[4]Corporal Michael J. Crescenz VA Medical Center, Surgical Services, Philadelphia, USA.

[5]Monell Chemical Senses Center, Philadelphia, USA

[6]Current address: Department of Microbiology & Molecular Genetics, Michigan State University, East Lansing, USA

[*]Correspondence: weisssr@pennmedicine.upenn.edu

Author contributions

Conceptualization: N.S.T, F.D.B, N.A.C. and S.R.W. Investigation: N.S.T, A.K.P, L.H.T. and A.D.M. Validation: N.S.T, A.K.P, L.H.T, A.D.M. and S.S. Resources: R.A.P.M., B.J.K., R.C., K.R., C.L., F.D.B., N.A.C., and S.R.W. Writing: N.S.T., F.D.B, N.A.C and S.R.W. Funding and supervision: S.N.T., F.D.B, N.A.C., S.R.W.

Abstract

The ongoing SARS-CoV-2 pandemic has been marked with emerging viral variants, some of which were designated as variants of concern (VOCs) due to their selection and rapid circulation in the human population. Here we elucidate functional features of each VOC linked to variations in growth during infection. Patient-derived primary nasal cultures grown at air-liquid-interface (ALI) were used to model upper-respiratory infection, and human lung epithelial cell lines used to model lower-respiratory infection. All VOCs replicated to higher titers than the ancestral virus, suggesting a selection for replication efficiency. In primary nasal ALI cultures, Omicron replicated to the highest titers at early time points, followed by Delta, paralleling comparative studies of patient samples. All SARS-CoV-2 viruses entered the cell primarily via a transmembrane serine protease 2 (TMPRSS2)-dependent pathway, and Omicron was more likely to use an endosomal route of entry. All VOCs overcame dsRNA-activated cellular responses including interferon signaling, oligoadenylate ribonuclease L (OAS-RNase L) degradation and protein kinase R (PKR) activation. Infections in nasal ALI resulted in damage to nasal cells such as a compromise of cell-barrier integrity and loss of nasal cilia and ciliary beating function, especially with Delta infections. Overall, Omicron replication was optimized for growth in the upper-respiratory system and least-favorable in the lower-respiratory cell line; and Delta was the most cytopathic for both upper and lower respiratory cells. Our findings highlight the functional differences among VOCs and illuminate distinct mechanisms of pathogenesis in infected individuals.

Significance Statement

In a comparative analysis of infections by SARS-CoV-2 ancestral virus and variants of concern including Alpha, Beta, Delta and Omicron, we found that variants are selected for efficiency in replication. In infections of patient-derived primary nasal cultures grown at air-liquid-interface (ALI) to model upper-respiratory infection, we show that Omicron reached highest titers at early

time points, a finding that is confirmed by parallel studies of patient sampling. In both primary nasal cells and lower-respiratory cell lines infections by Delta are most damaging to the cells as indicated by syncytia formation and loss of nasal ciliary function.

Key Words

SARS-CoV-2, COVID-19, variants of concern, primary nasal cells, spike cleavage, dsRNA

INTRODUCTION

The SARS-CoV-2 pandemic has been marked by evolution of the ancestral virus strains, Wuhan in the east and Washington in the west, into new variants. The World Health Organization has identified some of the variants that pose an increased risk for global public health as variants of concern (VOCs). Characteristics for VOCs include an increase in virus transmissibility and virulence, and/or a decrease in response to current vaccines, public health measures and therapeutics (1).

Four major VOC have emerged over the course of the pandemic. The Alpha VOC, B.1.1.7 pango lineage virus, was first documented in the United Kingdom in September 2020. The Beta VOC, B.1.351 pango lineage virus, was first documented in South Africa in May 2020. The Delta VOC, B.1.617.2 pango lineage virus, was first identified in India in October 2020. The B.1.1.529 pango lineage Omicron variant was first documented in South Africa in November 2021 (2); however, more recent reports suggest an earlier emergence. Since then, sub-variants have emerged from the Omicron lineage, including XBB.1.5 as the latest variant of interest.

Clinical retrospective studies report differences in patient outcomes among VOCs. Compared to the ancestral strain, patients infected with Delta and Alpha variants were associated with heightened disease severity, such as increase in oxygen requirement, longer hospitalization and morbidity (3). Patients infected with the Omicron variant appeared less likely to develop severe COVID, require hospitalization, and had lower rates of in-hospital mortality compared to Delta-infected patients but the assessment of these traits was confounded by the concomitant development of immunity from prior exposure and vaccination in these populations.

Variant-specific mutations to the ancestral SARS-CoV-2 genome are of interest for their potential roles in facilitating virus pathogenesis and spread. Many of the amino acid substitutions are found in the spike-encoding region of the SARS-CoV-2 genome. The spike (S) protein, composed of S1 and S2 subunits, binds to the host angiotensin converting enzyme 2 (ACE2) receptor to facilitate virus-host membrane fusion, virus entry, and modulates host

immune responses (4-6). Several studies attribute the enhanced immune evasion by the variants to substitutions in the spike protein. Amino acid substitutions that render the furin protease recognition site at the S1/S2 subunit junction in spike more basic have been associated with enhanced viral fitness for the Delta VOC, and to a lesser extent for the Alpha and Omicron variants (7). Deletions and substitutions within and adjacent to the furin protease recognition site have been associated with virus attenuation (8, 9). The role of mutations outside of the spike gene, although not as well characterized, likely also contribute to differences in pathogenesis. For example, mutations in the nucleocapsid gene have been associated with increased virus replication and pathogenesis (10).

To assess genome-wide differences between VOC in a controlled system, we compared molecular replication mechanism among full length, replication competent Alpha, Beta, Delta and Omicron VOCs to the ancestral Washington (WA-1) virus as wildtype (WT). All viruses were compared for replication kinetics and cellular responses to infections by VOCs in patient-derived primary nasal cells, with the goal of modelling the first step of infection. In addition, all experiments were repeated in cell lines derived from human lung tissues, including Calu-3 and A549, to represent subsequent infection of lower-respiratory cells. Our experiments clarify differences among variants in virus entry, virus replication, cell-to-cell spread of the virus, and activation of host innate immune responses and antiviral pathways.

This study adds to our understanding of SARS-CoV-2 variants in several ways. We compared the ancestral virus to Alpha, Beta, Delta and Omicron variants while many focus on a subset of this group. All experiments involve infections with authentic viruses in a BSL3 facility rather than the use of pseudoviruses or protein expression systems. Our experiments also quantify infectious viruses in addition to RNA copy numbers. While several useful animal models have been developed to study SARS-CoV-2 (11, 12) we find that our patient-derived airway epithelia model more faithfully reflects replication kinetics in the human nose, the first site of infection.

RESULTS

VOCs are selected for increased replication in upper respiratory cells.

SARS-CoV-2 infections are initiated in the upper respiratory system, so we sought to model this step by comparing infections in primary cells collected from nasal cavities of patients undergoing rhinologic evaluation. These cells were cultured on transwells at an air-liquid-interface (ALI) to recapitulate the natural state of the nasal epithelium, as we have reported previously (13). In virus growth curve assays, all SARS-CoV-2 viruses replicated to high titers (> 1x10^5 PFUs/mL), and all VOCs replicated to higher titers than WT (**Fig 1A**). Omicron reached the highest titers at early time points of infection, and WT generally produced the lowest titers compared to all variants. In Calu3 cells, a human lung epithelial cell line (**Fig 1B)** all viruses reached earlier peak titers [24-36 hours post infection (hpi)]. Similar to primary nasal cells, all VOCs replicated to higher titers than the ancestral WT in Calu3, suggesting that all VOCs were selected for more efficient replication than the ancestral SARS-CoV-2. However, it is interesting that Alpha and Beta VOCs reached significantly higher titers than Omicron earlier in Calu3 infections while Omicron reached significantly higher titers than Alpha/Beta/Delta in nasal cells. Together these results suggest that while all VOCs are more efficient in replication than the ancestral virus, Omicron is especially selected for heightened replication in nasal cells.

To ensure the integrity of our experiments, genomic RNA from each virus stock was sequenced and aligned against the Washington A reference genome before further analysis (**Fig S1**). The alignment confirmed that all viruses used in this study maintain the defining mutations of each lineage. Additionally, it confirmed that no new substitutions have become fixed at the known hotspots, including the furin protease recognition site (8).

Replication fitness at different temperatures may impact the potential for VOCs to cause seasonal outbreaks. To investigate whether the VOCs have adapted to colder temperatures, infections with WT, Delta and Omicron viruses were performed in ALIs at 33ºC and 37ºC (**Fig S3A**). We did not observe any significant differences in titer when comparing infections at both

temperatures up to 96 hpi, suggesting that SARS-CoV-2 replication is not temperature sensitive early in infection. However, we (13) and others have reported preference of the WT virus at 33°C at later times post infection.

SARS-CoV-2 viruses enter primarily by TMPRSS2-mediated plasma membrane fusion pathways.

During virus entry the SARS-CoV-2 spike protein interacts with TMPRSS2, a serine protease which cleaves and activates the spike to initiate fusion at the plasma membrane (14-16). It has been proposed that viruses with a disrupted furin protease recognition site at the S1/S2 boundary (RRAR in the ancestral virus) such as Omicron, can enter in a TMPRSS2-independent endosomal route in some cell types (17-21). To investigate entry via the plasma membrane or endosomal routes, we used the protease inhibitor Nafamostat that blocks TMPRSS2 and inhibits entry by this pathway. Upon treatment with Nafamostat we observed a large reduction in virus titer; and the difference did not change with a 10-fold increase (data not shown) in drug concentration (**Fig 2A**). Compared to untreated controls (DMSO) virus titer was inhibited by 95-99% for all viruses (**Fig 2B**). Omicron titer was affected the least, suggesting that Omicron is less dependent on the TMPRSS2-mediated entry pathway compared to the other SARS-CoV-2 viruses, and therefore may use the alternative endosomal route more than other VOCs. Similar results have been reported by others (15, 22-24). However, it is important to note that while Omicron is the least dependent VOC on the plasma membrane fusion pathway, it still enters primarily by this pathway in Calu3 cells.

The influence of furin protease cleavage on viral entry and cell-to-cell spread.

Cleavage of the spike protein at the furin recognition site facilitates both virus entry and cell-to-cell virus spread. The basic amino acids at the furin recognition site of spike protein, PRRAR in WT, recruit proteases necessary for the cleavage at the S1/S2 junction (25). This

region is sensitive to substitutions which influence infection and replication (8, 26-28). We hypothesized that the amino acid substitutions in VOCs that render the furin cleavage site more basic will be more efficiently cleaved, leading to increased cell-to-cell spread. Specifically, we hypothesize that the Delta virus, which encodes the most basic cleavage-site (RRRAR), will generate the most cleaved spike, followed by Alpha and Omicron (both HRRAR) generating equal levels of cleaved spike. Beta and WT, which encode S1/S2 site with the least basic charge (PRRAR), are expected to generate the least cleaved spike.

To measure the ratios of cleaved versus full-length spike protein levels among VOCs, a western blot was performed with protein lysates from infected primary nasal cells (**Fig 2C**). As predicted, quantification of the cleaved spike from 3 independent donors showed that Delta infections generated the highest proportion of cleaved spike (71%), followed by Alpha (52%), Omicron and Beta (~44% each), and WT (32%) (**Fig 2D**). The elevated levels of cleaved spike in infections by all VOCs compared to WT virus supports the idea that VOCs have evolved to optimize spread in human nasal cells. However, infection with Omicron produced the highest titers **(Fig 1A)** despite not generating the most cleaved spike (**Fig 2C-D**), indicating the importance of factors affecting other replication steps.

However, similar experiment in the VeroE6^{TMPRSS2} cell line did not yield the same ratios of cleaved spike (**Fig S2A**). While the highest ratio of cleaved-spike was produced with Delta infection (62% cleaved) as predicted and observed by others (29), contrary to our hypothesis, infection with the Beta virus generated the second most cleaved spike. Infections with Alpha and Omicron VOC generated different levels of cleaved spike despite sharing the same furin-cleavage site sequence (which was also true in primary nasal cells). These results suggest that while the strong basic charge at the furin-cleavage facilitates spike cleavage, there are other factors beyond the PRRAR sequence that facilitate cleavage. In addition, cell type-specific biology, e.g. variation in the abundances of various proteases, influences the cleavage of spike. As validation of our spike-cleavage assay we included infections with a positive control virus

(icWT) containing the ancestral PRRAR sequence and a negative control virus (icΔPRRA) containing a deletion of the PRRA sequence, both generated with the infectious cloning system (**Fig S2A**) (8). As expected, infections with both WT and icWT viruses, which both contain PRRAR, generated comparable ratios of S2 spike, while infection with the icΔPRRA virus lacking the PRRA sequence did not generate any cleaved S2 spike (**Fig S2A**).

An immunofluorescence staining assay (IFA) was used to visualize the spread of infection in A549^{ACE2} cells. Compared to the WT virus, Alpha and Delta infections generated strikingly larger syncytia with the classical clustering of nuclei in the middle (**Fig 2E**) which was supported by quantification of syncytia size measured by the area of nucleocapsid positive (green) clusters **(Fig 2F)**. Alpha and Omicron infections, despite sharing the same furin cleavage site, do not display similar levels of fusion. This again suggests that functional domains beyond the furin recognition site contribute to the extent of cell-to-cell spread. Together these data suggest that the Alpha and Delta VOCs are efficient at cell-to-cell spread, likely due to efficient spike cleavage and high fusogenic activity.

SARS-CoV-2 WT and VOC plaque morphology

Plaque assays were performed on VeroE6^{TMPRSS2} cells and plaque areas quantified (**Fig 3A-B**). The WT virus generated the largest plaques (average 1542 px^2) but also displayed the most range in plaque area, as reported by others (30). While all VOCs generated smaller plaques than WT, the plaques generated with Alpha and Delta VOCs were strikingly smaller (average of 211 px^2 and 231 px^2, respectively). It is intriguing that, in comparison to WT, Alpha and Delta generate smaller plaques even though they produce higher titers of virus in growth curves (**Fig 1A-B**) and larger syncytia (**Fig 2E-F**). This demonstrates that for SARS-CoV-2, plaque size does not necessarily correlate with replication and cell-to-cell spread, an observation made previously about murine coronavirus strains (31).

The differences in infectious virus production in titer assays, despite comparable levels of intracellular genome replication by RT-qPCR (**Fig S2B**), prompted us to quantify the particle-to-PFU ratio among VOCs. Compared to the WT virus, all VOCs, except Delta, secreted significantly fewer genomes per infectious virus (**Fig 3C**), suggesting that Alpha, Beta and Omicron VOCs are more efficient at producing infectious virus. The Delta VOC genome-to-PFU ratio was not significantly different from WT.

Double-stranded (ds)RNA-activated innate immune responses to SARS-CoV-2 variants

dsRNAs generated during the replication of RNA viruses, including coronaviruses, are detected by host cells and elicit antiviral responses. There are three major cytosolic sensors of dsRNAs that induce innate immune responses (32). Detection of coronavirus dsRNA by MDA5 leads to induction of type-I and type-III interferons (IFNs) and activation of interferon-stimulated genes (ISG), many of which encode proteins with antiviral activities. Sensing of dsRNA by oligoadenylate synthetases (OASs) leads to production of 2',5'-oligoadenylates, which activate RNase L to degrade host and viral ssRNA. Activation by protein kinase R (PKR) leads to dimerization and autophosphorylation followed by phosphorylation of p-eIF2α and inhibition of translation. Both RNase L and PKR activation lead to reduced virus replication, apoptosis and inflammation (33). Thus differential responses to these pathways are a potential explanation for the differences in pathogenesis of the VOCs.

To compare the induction of interferon (INF) pathway among the SARS-CoV-2 viruses, RT-qPCR was used after infection to quantify gene expression of type-I IFN (interferon beta, *IFNB*), type-III IFN (interferon lambda 1, *IFNL1*), and interferon induced genes (ISGs) including 2'-5'-oligoadenylate synthetase 2 (*OAS2)* and interferon induced protein with tetratricopeptide repeats 1 (*IFIT1)* (**Fig 4**). To ensure productive virus replication SARS-CoV-2 nsp12 (RNA dependent RNA polymerase) levels were quantified from infected cell lysates (**Fig 4A, i**). SINV infection was used as positive control as we have observed it to elicit strong innate immune

responses (32). In A549^{ACE2} cells, we observed that WT induced high levels of *INFB* and *IFNL1* genes, but these IFN responses were not proportionally elevated with VOCs (**Fig 4A ii-iii**). With ISGs such as *OAS2* and *IFIT1* we observed comparable expressions with WT and Beta infections compared to Alpha, Delta and Omicron (**Fig 4A iv-v**). These ratios of responses were observed in two independent experiments, and do not correlate with virus genome copy levels (**Fig 4A i**) suggesting a reliable quantification of innate-immune responses induced in A549 cell infections that is not skewed by viral RNA copy numbers. In Calu3 cells we observed that Beta infection generated significantly greater interferon response than ancestral WT or other VOCs (**Fig 4B ii-iii**); however, this patter was not repeated with ISGs (**Fig 4B iv-v**). In primary nasal cells, while we did not observe any striking differences among viruses, we did observe that Omicron infection showed a trend toward higher levels of interferon gene expression over other VOCs in multiple experiments (**Fig 4C**). Consistent with these data, previous studies comparing interferon induction between Delta and Omicron infections in cell lines have also reported greater induction with Omicron (34, 35). While we do observe higher IFN induction with Omicron infection compared to other variants and ancestral virus, the lack of a statistically significant difference may be due to elevated basal level of IFN in primary nasal cells that thwarts high-level induction (32).

The activation of the PKR pathway by SARS-CoV-2 infections was measured by western blot (**Fig 5A-B**). In primary nasal cells phosphorylated-PKR (p-PKR) was detected with all infections with highest levels observed with Omicron infection, suggesting all SARS-CoV-2 viruses activate the PKR pathway (**Fig 5A**). Phosphorylated-eIF2α was also detected above mock levels with all infections with highest levels observed with Beta and Delta infection (**Fig 5A**). In A549^{ACE2} cells, WT and Omicron infections resulted in phosphorylation of PKR, while Alpha, Beta and Delta infections did not (**Fig 5B**). Reduced levels of PKR with Alpha, Beta and Delta infections were detected reproducibly in multiple western blots and this observation is not due to reduced replication of virus as confirmed by comparable nucleocapsid signal and titer

(**Fig 5B and S2C**). Infections by all viruses generated p-eIF2α, with the highest level with Alpha and lowest with Delta infection. Together these results suggest that all SARS-CoV-2 infections in A549 cells induce the PKR pathway (**Fig 5A-B**).

The activation of the RNase L pathway can be inferred by measuring rRNA degradation (**Fig 5C**). A549^{ACE2} cells were infected with SARS-CoV-2 WT, VOCs and Sindbis Virus (SINV) as a positive control, and rRNA cleavage quantified using a Bioanalyzer. Compared to mock-infected cells (RIN 9.6), SINV infection was associated with a strong accumulation of rRNA degradation products (arrows), as expected (RIN 9.0). In the comparison of SARS-CoV-2 viruses, Beta infection generated the highest levels of rRNA degradation products (RIN 6.2), followed by WT (RIN 8.5) and Alpha (RIN 8.3), which showed similar levels. The low levels of rRNA degradation in Delta (RIN 9.) and Omicron (RIN 9.5) infection could be due to delayed progression of infection, as indicated by lower N levels (**Fig 5C**) and titer (**Fig S2C**), rather than a muted response by the RNase L pathway. These comparisons suggest that SARS-CoV-2 infections, in A549 cells, activate the OAS-RNase L pathway to a similar extent.

Damage to upper-respiratory cells associated with Delta infection.

Infection by SARS-CoV-2 can last for prolonged periods, raising the question of possible damage to infected tissue. To compare damage caused by the different variants we measured the transepithelial electrical resistance (TEER), which measures electrical resistance across the cell membranes that is maintained by intact cell-to-cell junctions. In general, TEER values rise as the ALI cultures differentiate and become more confluent; however, any compromise to cell-to-cell barrier integrity or loss of ion transport across the membrane results in a loss of TEER value. We found that while all VOCs display an increase in TEER resistance from 0-48hpi, there is a drop in TEER at 48-96hpi, and the most dramatic and significant loss of TEER was measured with Delta infection (**Fig 6A**). This observation suggests that Delta and Omicron

infections are compromising cell-to-cell barrier integrity and biological functions of nasal cells more severely than other variants.

The heterogenous nasal cell cultures include ciliated cells; the cilia facilitate transport and clearance of mucus that is generated in the nasal cavity. Ciliary beat frequency can be measured to assay activity and function of cilia as well as overall health of ALI cultures. Compared to mock cells, infected ALI cultures displayed a reduced frequency of ciliary beating (**Fig 6B**). This phenotype was the most notable during Alpha and Delta infections, which display 75% reduction of cilia beating frequency, and 80% reduction in number of beating cilia compared to mock (**Fig 6B and 6E**). This suggests that SARS-CoV-2 infection compromises ciliary beating function in the nasal cell cultures, with different potency among variants.

Confocal microscopy was used to visualize the spread of infection further. During early infection (24hpi) we observed that infected cells colocalized with a cilia marker, confirming that SARS-CoV-2 infects ciliated cells (**Fig 6C**) (13). Additionally, only a fraction (<5%) of the ciliated cells were infected at this early time point. During late infection (96hpi) we observed a vast spread of infection throughout the ALI culture. We also observed that Delta infected ALI cultures showed some small syncytia-like clusters (**Fig 6C**, arrow), although not as pronounced as in lower respiratory cell lines (**Fig 2E**). The loss of the cytoskeletal marker, phalloidin, between cells in this cluster is further evidence of formation of syncytia (**Fig S3C**). At higher magnification we observed that during late infection (96hpi), Delta infected cells are negative for the cilia marker, suggesting deciliation of the infected cells (**Fig 6D**). Using live microscopy and point-analysis, we also observed a reduction in the area where beating cilia could be detected (**Fig 6E**), further documenting deciliation. Together these results suggest that among the SARS-CoV-2 viruses, Delta VOC causes the most cytopathic infection in human nasal cells.

Population surveillance of SARS-CoV-2 VOCs

Given our goal of understanding molecular correlates of differences among variants, and the results described above, we next investigated whether infection with different SARS-CoV-2 variants were associated with higher viral RNA production as reported by qPCR assays on clinical specimens. Samples were obtained from a program that paired viral whole genome sequencing with collection of clinical metadata, so that relative viral RNA levels were linked to the variant calls (36). Samples were analyzed from 2,722 infected participants. Due to the low prevalence of Beta infection in the region our data does not include this VOC. Data from several sampling and analysis pipelines were combined, so a Bayesian analytical framework was used to control confounders and assess the significance of differences among variants (**Fig 7**). Relative abundance was quantified as cycle of threshold (Ct) in the qPCR, so that lower values indicate higher abundances.

We found that Delta specimens had Ct values that were estimated to be on average 1.77 Ct lower than Alpha (95% Credible Interval (CrI): 0.70, 2.89) and 0.43 Ct lower than Omicron (95% CrI: 0.15, 0.72). Omicron was estimated to have a Ct 1.35 cycles lower than Alpha (95% CrI: 0.28, 2.42). Thus, Delta was consistently found to have a lower Ct and thus higher numbers of RNA copies in infected human participants, followed by Omicron and Alpha. This is consistent with published studies of patient samples (37-40) and matches our findings that Delta and Omicron VOCs are most efficient at replicating in primary nasal cells.

Discussion

The COVID-19 pandemic has been marked with emergence of SARS-CoV-2 variants including Alpha, Beta, Delta and Omicron, which were designated as variants of concern (VOC) due to their heightened risk to the population. Infection with different VOCs have shown notable differences in patient health outcomes (41) but understanding of the differences in viral biology accounting for these differences is incomplete. A comparative mechanistic analysis of SARS-CoV-2 variants is necessary to delineate the virus-host biology driving pathogenesis and to help predict pathogenicity of future variants. Our findings parallel and provide mechanistic insight into retrospective human studies (41, 42) which showed that infections with Delta virus are most pathogenic, while Omicron is less pathogenic and instead selected for better replication (42).

Our findings focus attention on the differences in infections among SARS-CoV-2 viruses in both cell lines and primary cells. The cell lines used include A549 and Calu3, which allow us to compare infection in lower respiratory tract models. However, a caveat of such comparison is the effects of primary cells versus cell lines derived from carcinomas to the observations. A strength of our study lies in analysis of infection in patient-derived primary nasal cells which are the primary site of infection and model the upper respiratory tract (32). Unlike cell lines or animal models, our findings with the primary nasal cell model parallel human epidemiological studies in the comparison of infections by the different variants, in that, in both models Delta and Omicron were selected for efficient replication than other SARS-CoV-2 VOCs.

A consistent observation throughout our studies is that SARS-CoV-2 infections with the Delta variant are most damaging in both upper and lower respiratory model systems. This could be attributed to the polybasic furin cleavage site on the Delta spike protein which can recruit proteases to facilitate spike cleavage. However, Alpha and Omicron viruses that carry an identical furin cleavage site sequence generate different levels of cleaved spike, virus spread and cellular damage. Thus our results indicate that factors in addition to the cleavage site play a role in these processes. Sequence and structure-based bioinformatics studies have proposed

that mutations in Omicron encoding substitutions at the S1/S2 site may help evade recognition by proteases and prevent syncytia formation (43).

Differences in innate immune responses to infections by different VOCs have been studied extensively. In A549 cells, we have shown that all VOCs exhibit a reduced *IFNB* and *IFNL* gene response compared to the ancestral strain. However, in Calu3 cells, Beta infection elicited a stronger interferon response that surpassed other SARS-CoV-2. Additionally, IFN induction was much higher in A549 and Calu3 cells compared to primary sinonasal cells. These variations may be explained by several factors. First, different cell types have different capacities for generating interferon responses. For example, it has been shown that nasal cells have elevated basal levels of interferon gene expression and thus induction may be blunted (32). Second, the level of innate responses may correlate with viral load in cells, and different VOCs replicate to different titers. Overall, our conclusion is that many factors influence IFN responses, and it is important for future studies to account for levels of virus replication, cell types, basal IFN gene expression and mode of induction such as an infection versus overexpression in the analysis.

Primary human nasal cells grown at an air-liquid-interface are a powerful model to recapitulate coronavirus infections of the upper respiratory system (32, 44). Previous studies have validated SARS-CoV-2 infections in such models ((13, 45, 46). Here we were able to characterize specific forms of cellular damage in ciliated cells by different VOCs. Immunofluorescence analysis shows that Delta is the most cytopathic VOC, followed by Omicron and Alpha. This order was also observed with levels of spike cleavage, suggesting that in nasal cells Delta may spread by cell-to-cell fusion more than other VOCs. Analysis of TEER also identified Delta as most damaging to cell barrier integrity, followed by Omicron. However, further analysis suggests that Delta and Alpha caused the greatest loss of ciliary beating function. Therefore, while Delta infection compromises both functions, Omicron is detrimental to cell-barrier integrity but not the rate of ciliary beating, and Alpha infection eliminates ciliary

beating but not cell-barrier integrity. This contrast distinguishes separate mechanisms involved in maintaining cell barrier integrity versus mechanisms of ciliary beating which has not been reported previously. It would be interesting to compare these differences at the cellular level to variant-specific patient symptoms.

In primary nasal cells we observed that Delta and Omicron reach higher titers faster, while WT produced the lowest titer. By contrast, in the Calu3 cell line, the earlier VOCs such as Alpha and Beta reached higher titers earlier. These results suggest that SARS-CoV-2 is evolving for efficient replication in the upper respiratory system. This observation concurs with clinical studies that report Omicron infections induce more upper-respiratory symptoms with reduced pathogenic manifestation (47, 48). Epidemiological studies have also reported lower introductory reproduction rates (R0) for the later variants, especially Omicron, compared to the ancestral viruses (49). These observations suggest future variants may continue to be selected for upper-respiratory infections and a general decrease in pathogenicity.

Our study has several weaknesses. Some differences among variants may be due to analysis using cell lines instead of primary cells. Studies of Ct values from patient samples are complicated by use of different analytical technologies during different stages of the epidemic.

The currently circulating SARS-CoV-2 virus is likely to continue to evolve. The findings in this study provide a comprehensive comparison of VOCs to date in cell culture, clarifying important differences in virus-host biology among SARS-CoV-2 variants affecting pathogenesis. These findings can be applied to understand and predict replication, spread and immunogenicity of future variants.

Materials and Methods

Viruses: The following viruses were obtained from BEI resources, WT/USA-WA1/2020 strain NR-52281 and Alpha NR-54000. Delta and Omicron were isolated from a patient sample. All viruses were grown in VeroE6^{TMPRSS2} cells and titers were quantified by plaque assay on VerE6^{TMPRSS2} monolayer overlayed with 0.1% agarose and stained with 10% crystal violet. All viruses were sequence verified using the POLAR protocol using an Illumina NextSeq instrument with a 74 × 74 paired-end sequencing on a 150 cycle MID output cartridge (50). Infections were performed at MOI=0.1, unless otherwise specified, in serum-free DMEM for 1-hour, followed by refeed of cellular media for the duration of the experiment. For growth curve experiments, virus supernatant was collected at noted hours post infection (hpi) and quantified by plaque assay. For intracellular virus, cells were collected in DMEM and subject to 3 freeze-thaw cycles to release intracellular virus.

Cell lines: VeroE6^{TMPRSS2} (African green monkey kidney) cells were maintained in DMEM (Gibco cat. No. 11965) with 10% fetal bovine serum (FBS), 100 U/ml penicillin, 100 ug/ml streptocymic, 50 ug/ml gentamicin, 1 mM sodium pyruvate, and 10 mM HEPES. Human A549^{ACE2} cells were cultured in PRMI 1640 (Gibco cat. No. 11875), 10% FBS, 100 U/ml of penicillin and 100 ug/ml streptomycin. Human Calu3 cells (clone HTB-55) were maintained in MEM media with 10% FBS.

Genomes/PFU: Calu3 cells were infected with respective viruses at MOI 0.1, at 24hpi virus supernatant was collected for quantification. PFUs were measured by plaque assay. Genomes were measured by extracting RNA from the supernatant and performing RT-qPCR with primers for SARS-CoV-2 genome nsp12/RdRp.

RNA collection: Cells were lysed at indicated hours post infection in Buffer RLT (Qiagen cat. No. 79216) followed by RNA was extracted using the RNeasy Plus Mini Kit (Qiagen cat. No. 74004). Cell-free supernatant was lysed with AVL buffer (Qiagen cat. No 19073) and RNA was extracted with QIAmp Viral RNA Mini Kit (Qiagen 52904).

RT-qPCR: Protocol for RT-qPCR was previously described before and briefly outlined here (51). RNA was reverse transcribed into cDNA with a High Capacity cDNA Reverse Transcriptase Kit (Applied Biosystems). Target cDNA was amplified using specific primers, iQ SYBR Green Supermix (Bio-Rab) and QuantStudio 3 PCR system (Thermo Fisher). Gene expression is displayed as fold change over mock-infected samples ($\Delta(\Delta Ct)$ = ΔCt infected sample - ΔCt mock sample) normalized over 18s rRNA (ΔCt = Ct gene of interest - Ct 18S rRNA). Graphed values represent $2^{-\Delta(\Delta Ct)}$ obtained from the mean of biological triplicates of each condition and technical triplicates of each sample. Host gene expression was quantified with the following primers (forward sequence/ reverse sequence): INFB (GTCAGAGTGGAAATCCTAAG/ CAGCATCTGCTGGTTGAAG), IFNL1 (CGCCTTGGAAGAGTCACTCA/ GAAGCCTCAGGTCCCAATTC), OAS2 (TTCTGCCTGCACCACTCTTCACGAC/ GCCAGTCTTCAGAGCTGTGCCTTTG), IFIT1 (TGGTGACCTGGGGCAACTTT/ AGGCCTTGGCCCGTTCATAA) and 18S rRNA (TTCGATGGTAGTCGCTGTGC/ CTGCTGCCTTCCTTGAATGTGGTA). Virus genomes were quantified in reference to a standard curve, with primers for SARS-CoV-2 genomic nsp12/RdRp (GGTAACTGGTATGATTTCG/ CTGGTCAAGGTTAATATAGG).

Graphical visualization, quantification and statistics: Graphs were generated using Prism software. Statistics were also performed with Prism software with specific tests stated with each experiment. Plaque area quantification, syncytia area quantification and western blot quantification were performed with ImageJ software.

Protease treatments: Nafamostat (20uM, 200uM) was used for protease inhibition (52). Calu3 cells were pre-treated for 2 hours with appropriate concentrations of drug in the cell media. Infections were performed at MOI=0.1 for 1hour, after which inoculum was replaced with Calu3 media plus drug for 1 additional hour of post-treatment. In experimental conditions, cell media was replaced with drug-free media for the remainder of the experiment. For positive control, drug concentration was maintained in the media for 4hours of post-treatment. For negative

control, no drug was included in the media and DMSO media (dimethyl sulfoxide, Thermo Scientific cat no J66650)) was used instead. Supernatants were collected at 16hpi for quantification by plaque assay. Percent inhibition was calculated as fraction of virus titer after drug treatment over virus titer without drug treatment.

rRNA degradation assay: RNA integrity was analyzed on a chip with Aligent 2100 Bioanalyzer using the Aligent 196 RNA 6000 Nano Kit (Cat #: 5067- 197 1511)

Western Immunoblot: Cell lysates were washed in PBS and harvested in lysis buffer (1% NP-40, 2mM EDTA, 10% glycerol, 150mM NaCl, 50mM Tris-HCl, protease inhibitor (Roche complete mini EDTA-free protease inhibitor), phosphatase inhibitor (Roche PhosStop easy pack). After 20 minutes of lysis on ice, samples were centrifuged to remove cell debris. Lysates were denatured at 95C for 5 minutes and stored for analysis. Protein lysates were separated on 5-15% SDS-PAGE gradient gel and transferred onto a PVDF membrane. Membrane blots were blocked with 5% nonfat milk or 5% BSA, and probed with appropriate primary antibodies overnight at 4C, and secondary antibodies for 2h at room temperature. Blots were exposed with chemiluminescent substrate (Thermo Scientific Cat. No. 34095 or 34080). Blots were stripped (Thermo Scientific cat no 21059) and reblotted as needed.

Primary sinonasal ALI cultures: Sinonasal cells were obtained from patient donors with informed consent, per protocol approved by the University of Pennsylvania Institutional Review Board (protocol #800614). Specimens were dissociated and grown to 80% confluence in in PneumaCult™-ALI Medium (STEMCELL Technologies 05001) supplemented with heparin (STEMCELLl Technologies 07980) and hydrocortisone. A detailed protocol was described previously (32, 53).

Transepithelial electrical resistance (TEER): TEER measurements were obtained with the EVOM apparatus, in PBS supplemented with calcium and magnesium. TEER measurements were obtained for all ALI transwells pre-infection (0hpi) and post-infection (48hpi and 96hpi). ∆TEER is the difference in TEER from 0hpi to 48hpi, and 48hpi to 96hpi.

Cilia beat frequency and beating cilia: Live microscopy movies of ALI cultures were obtained with a 20x objective on a brightfield microscope. Movie segments were analyzed on SAVA system to obtain cilia beat frequency (54). Beating cilia was obtained with single point analysis. Graphed values are an average of 3 ALI cultures per condition and 4 regions of interest per culture.

Immunofluorescence: Calu3 cells were seeded on coverslips and infected at confluency at MOI0.1. At 24hpi samples were fixed with 4% paraformaldehyde for 15 minutes, followed by permeabilization with 0.5% trypsin for 10 minutes. Samples were blocked with 1% BSA, followed by incubation with primary antibodies for 2 hours at room temperature, and secondary antibodies for 1 hour at room temperature. Antibodies used include DAPI, Nucleocapsid (1:500, gift from Dr. Tony Schountz, Colorado State University, Fort Collins, CO, USA), Alexa-488 goat anti-mouse (1:1000, Thermo Scientific cat no A11011). Images were obtained with a 60x objective on a Nikon Ti-8 brightfield microscope. For ALI visualization, infections were performed at MOI 0.1 followed by fixation of transwells at indicated time points with 4% paraformaldehyde for 20 minutes. Images were captured on a confocal microscope and displayed as overlay projections.

Ct analysis of Delaware Valley surveillance: Samples were collected from the Delaware Valley under University of Pennsylvania IRB protocol no. 823392, CDC BAA 200-2021-10986 and CDC 75D30121C11102/000HCVL1-2021-55232. RNA samples were analyzed by whole genome sequencing as described previously (36, 55). Ct values were obtained from patient records. Clinical viral RNA level measured by cycle threshold (Ct) was predicted using a Bayesian regression model as implemented in BRMS using a thin plate spline for time since variant first detected and random effect of qPCR machine, specimen type, and variant of sample.

$$Ct_i \sim s(t_i) + \lambda_i + \alpha_v + \beta_m$$

Where Ct_i is an estimate of a sample's Ct value. $s(t_i)$ is a thin plate regression spline calculated to account for variations over time for all variant's introduction. λ_i is the effect on sample location on either upper or lower respiratory tract. α_v is the effect for a given variant, and β_m is the effect for a given qPCR protocol.

2,722 SARS-CoV-2 positive participants had clinical Ct data collected and were sequenced through whole-genome sequencing from 2/15/2021 to 7/18/2022. The supplemental table contains metadata and sequence accessions used in this analysis. One of six qPCR protocols were used (Cepheid GeneXpert, Cobas8800, Cobas Liat, DiaSorin MDX, Saliva COVID, or ThermoFisher Amplitude). One of five variant categories were assigned from whole genome sequencing (Alpha, Delta, Omicron, other variant, pre-variant of concern).

Acknowledgements

We thank Dr. Paul Planet for the Delta variant sample, Drs Peter Hewins and Kellie Jurado for the Beta variant, Dr. Pei Young Shi for the icWT and icPRRA deletion viruses. We also thank Drs. David W. Kennedy, James N. Palmer, Nithin D. Adappa, and Michael A. Kohanski for aid in the collection of nasal tissue for establishing primary nasal epithelial cultures. This work was supported by National Institutes of Health grants R01 AI140442 (SRW) and R01AI169537 (SRW&NAC); Department of Veterans Affairs Merit Review 1-I01-BX005432-01 (NAC&SRW). NST was supported in part by T32NS43126-18. This work was also supported by the Penn Center for Research on Coronaviruses and Other Emerging Pathogens (SRW).

Disclosures

Susan R Weiss is on the Scientific Advisory Board of Ocugen, Inc. and consults for Powell Gilbert LLP. Noam A Cohen consults for GSK, AstraZeneca, Novartis, Sanofi/Regeneron, Oyster Point Pharmaceuticals; has US Patent “Therapy and Diagnostics for Respiratory Infection” (10,881,698 B2, WO20913112865) and a licensing agreement with GeneOne Life Sciences.

References

1. Carabelli AM, Peacock TP, Thorne LG, Harvey WT, Hughes J, de Silva TI, et al. SARS-CoV-2 variant biology: immune escape, transmission and fitness. Nature Reviews Microbiology. 2023;21(3):162-77.
2. O'Toole Á, Scher E, Underwood A, Jackson B, Hill V, McCrone JT, et al. Assignment of epidemiological lineages in an emerging pandemic using the pangolin tool. Virus Evolution. 2021;7(2).
3. Ong SWX, Chiew CJ, Ang LW, Mak TM, Cui L, Toh MPHS, et al. Clinical and Virological Features of Severe Acute Respiratory Syndrome Coronavirus 2 (SARS-CoV-2) Variants of Concern: A Retrospective Cohort Study Comparing B.1.1.7 (Alpha), B.1.351 (Beta), and B.1.617.2 (Delta). Clinical Infectious Diseases. 2021;75(1):e1128-e36.
4. Mannar D, Saville JW, Sun Z, Zhu X, Marti MM, Srivastava SS, et al. SARS-CoV-2 variants of concern: spike protein mutational analysis and epitope for broad neutralization. Nature Communications. 2022;13(1):4696.
5. Li F. Structure, Function, and Evolution of Coronavirus Spike Proteins. Annu Rev Virol. 2016;3(1):237-61.
6. Diamond MS, Kanneganti T-D. Innate immunity: the first line of defense against SARS-CoV-2. Nature Immunology. 2022;23(2):165-76.
7. Liu Y, Liu J, Johnson BA, Xia H, Ku Z, Schindewolf C, et al. Delta spike P681R mutation enhances SARS-CoV-2 fitness over Alpha variant. Cell Rep. 2022;39(7):110829.
8. Johnson BA, Xie X, Bailey AL, Kalveram B, Lokugamage KG, Muruato A, et al. Loss of furin cleavage site attenuates SARS-CoV-2 pathogenesis. Nature. 2021;591(7849):293-9.
9. Sasaki M, Uemura K, Sato A, Toba S, Sanaki T, Maenaka K, et al. SARS-CoV-2 variants with mutations at the S1/S2 cleavage site are generated in vitro during propagation in TMPRSS2-deficient cells. PLoS Pathog. 2021;17(1):e1009233.
10. Johnson BA, Zhou Y, Lokugamage KG, Vu MN, Bopp N, Crocquet-Valdes PA, et al. Nucleocapsid mutations in SARS-CoV-2 augment replication and pathogenesis. PLoS Pathog. 2022;18(6):e1010627.
11. Rodriguez-Rodriguez BA, Ciabattoni GO, Duerr R, Valero-Jimenez AM, Yeung ST, Crosse KM, et al. A neonatal mouse model characterizes transmissibility of SARS-CoV-2 variants and reveals a role for ORF8. Nat Commun. 2023;14(1):3026.
12. Mohandas S, Shete A, Kumar A, Wakchaure K, Rai V, Mote C, et al. Comparative pathogenicity of BA.2.12, BA.5.2 and XBB.1 with the Delta variant in Syrian hamsters. Front Microbiol. 2023;14:1183763.
13. Otter CJ, Fausto A, Tan LH, Khosla AS, Cohen NA, Weiss SR. Infection of primary nasal epithelial cells differentiates among lethal and seasonal human coronaviruses. Proc Natl Acad Sci U S A. 2023;120(15):e2218083120.
14. Yamamoto M, Kiso M, Sakai-Tagawa Y, Iwatsuki-Horimoto K, Imai M, Takeda M, et al. The Anticoagulant Nafamostat Potently Inhibits SARS-CoV-2 S Protein-Mediated Fusion in a Cell Fusion Assay System and Viral Infection In Vitro in a Cell-Type-Dependent Manner. Viruses. 2020;12(6).
15. Jäger N, Hoffmann M, Pöhlmann S, Krüger N. Nafamostat-Mediated Inhibition of SARS-CoV-2 Ribosomal Frameshifting Is Insufficient to Impair Viral Replication in Vero Cells. Comment on Munshi et al. Identifying Inhibitors of -1 Programmed Ribosomal Frameshifting in a Broad Spectrum of Coronaviruses. Viruses 2022, 14, 177. Viruses. 2022;14(7).
16. Koch J, Uckeley ZM, Doldan P, Stanifer M, Boulant S, Lozach PY. TMPRSS2 expression dictates the entry route used by SARS-CoV-2 to infect host cells. Embo j. 2021;40(16):e107821.
17. Zhu Y, Feng F, Hu G, Wang Y, Yu Y, Zhu Y, et al. A genome-wide CRISPR screen identifies host factors that regulate SARS-CoV-2 entry. Nature Communications. 2021;12(1):961.
18. Belouzard S, Millet JK, Licitra BN, Whittaker GR. Mechanisms of coronavirus cell entry mediated by the viral spike protein. Viruses. 2012;4(6):1011-33.

586 19. Willett BJ, Grove J, MacLean OA, Wilkie C, De Lorenzo G, Furnon W, et al. SARS-CoV-2 Omicron is
587 an immune escape variant with an altered cell entry pathway. Nature Microbiology. 2022;7(8):1161-79.
588 20. Peacock TP, Brown JC, Zhou J, Thakur N, Sukhova K, Newman J, et al. The altered entry pathway
589 and antigenic distance of the SARS-CoV-2 Omicron variant map to separate domains of spike protein.
590 bioRxiv. 2022:2021.12.31.474653.
591 21. Rudraraju R, Gartner MJ, Neil JA, Stout ES, Chen J, Needham EJ, et al. Parallel use of human stem
592 cell lung and heart models provide insights for SARS-CoV-2 treatment. Stem Cell Reports.
593 2023;18(6):1308-24.
594 22. Li K, Meyerholz DK, Bartlett JA, McCray PB, Jr. The TMPRSS2 Inhibitor Nafamostat Reduces SARS-
595 CoV-2 Pulmonary Infection in Mouse Models of COVID-19. mBio. 2021;12(4):e0097021.
596 23. Hoffmann M, Kleine-Weber H, Schroeder S, Krüger N, Herrler T, Erichsen S, et al. SARS-CoV-2
597 Cell Entry Depends on ACE2 and TMPRSS2 and Is Blocked by a Clinically Proven Protease Inhibitor. Cell.
598 2020;181(2):271-80.e8.
599 24. Meng B, Abdullahi A, Ferreira IATM, Goonawardane N, Saito A, Kimura I, et al. Altered TMPRSS2
600 usage by SARS-CoV-2 Omicron impacts infectivity and fusogenicity. Nature. 2022;603(7902):706-14.
601 25. Whittaker GR. SARS-CoV-2 spike and its adaptable furin cleavage site. The Lancet Microbe.
602 2021;2(10):e488-e9.
603 26. Vu MN, Lokugamage KG, Plante JA, Scharton D, Bailey AO, Sotcheff S, et al. QTQTN motif
604 upstream of the furin-cleavage site plays a key role in SARS-CoV-2 infection and pathogenesis. Proc Natl
605 Acad Sci U S A. 2022;119(32):e2205690119.
606 27. Lubinski B, Fernandes MHV, Frazier L, Tang T, Daniel S, Diel DG, et al. Functional evaluation of
607 the P681H mutation on the proteolytic activation of the SARS-CoV-2 variant B.1.1.7 (Alpha) spike.
608 iScience. 2022;25(1):103589.
609 28. Navaratnarajah CK, Pease DR, Halfmann PJ, Taye B, Barkhymer A, Howell KG, et al. Highly
610 Efficient SARS-CoV-2 Infection of Human Cardiomyocytes: Spike Protein-Mediated Cell Fusion and Its
611 Inhibition. J Virol. 2021;95(24):e0136821.
612 29. Khatri R, Siddqui G, Sadhu S, Maithil V, Vishwakarma P, Lohiya B, et al. Intrinsic D614G and
613 P681R/H mutations in SARS-CoV-2 VoCs Alpha, Delta, Omicron and viruses with D614G plus key
614 signature mutations in spike protein alters fusogenicity and infectivity. Med Microbiol Immunol.
615 2023;212(1):103-22.
616 30. Shiliaev N, Lukash T, Palchevska O, Crossman David K, Green Todd J, Crowley Michael R, et al.
617 Natural and Recombinant SARS-CoV-2 Isolates Rapidly Evolve In Vitro to Higher Infectivity through More
618 Efficient Binding to Heparan Sulfate and Reduced S1/S2 Cleavage. Journal of Virology.
619 2021;95(21):e01357-21.
620 31. Phillips JM, Gallagher T, Weiss SR. Neurovirulent Murine Coronavirus JHM.SD Uses Cellular Zinc
621 Metalloproteases for Virus Entry and Cell-Cell Fusion. J Virol. 2017;91(8).
622 32. Li Y, Renner DM, Comar CE, Whelan JN, Reyes HM, Cardenas-Diaz FL, et al. SARS-CoV-2 induces
623 double-stranded RNA-mediated innate immune responses in respiratory epithelial-derived cells and
624 cardiomyocytes. Proceedings of the National Academy of Sciences. 2021;118(16):e2022643118.
625 33. Zhao L, Jha BK, Wu A, Elliott R, Ziebuhr J, Gorbalenya AE, et al. Antagonism of the interferon-
626 induced OAS-RNase L pathway by murine coronavirus ns2 protein is required for virus replication and
627 liver pathology. Cell Host Microbe. 2012;11(6):607-16.
628 34. Bojkova D, Widera M, Ciesek S, Wass MN, Michaelis M, Cinatl J. Reduced interferon antagonism
629 but similar drug sensitivity in Omicron variant compared to Delta variant of SARS-CoV-2 isolates. Cell
630 Research. 2022;32(3):319-21.
631 35. Shalamova L, Felgenhauer U, Wilhelm J, Schaubmar AR, Büttner K, Schoen A, et al. Omicron
632 variant of SARS-CoV-2 exhibits an increased resilience to the antiviral type I interferon response. PNAS
633 Nexus. 2022;1(2).

634 36. Marques AD, Sherrill-Mix S, Everett JK, Reddy S, Hokama P, Roche AM, et al. SARS-CoV-2
635 Variants Associated with Vaccine Breakthrough in the Delaware Valley through Summer 2021. mBio.
636 2021;13(1):e0378821.
637 37. Woodbridge Y, Amit S, Huppert A, Kopelman NM. Viral load dynamics of SARS-CoV-2 Delta and
638 Omicron variants following multiple vaccine doses and previous infection. Nature Communications.
639 2022;13(1):6706.
640 38. von Wintersdorff CJH, Dingemans J, van Alphen LB, Wolffs PFG, van der Veer BMJW, Hoebe
641 CJPA, et al. Infections with the SARS-CoV-2 Delta variant exhibit fourfold increased viral loads in the
642 upper airways compared to Alpha or non-variants of concern. Scientific Reports. 2022;12(1):13922.
643 39. King KL, Wilson S, Napolitano JM, Sell KJ, Rennert L, Parkinson CL, et al. SARS-CoV-2 variants of
644 concern Alpha and Delta show increased viral load in saliva. PLoS One. 2022;17(5):e0267750.
645 40. Fall A, Eldesouki RE, Sachithanandham J, Morris CP, Norton JM, Gaston DC, et al. The
646 displacement of the SARS-CoV-2 variant Delta with Omicron: An investigation of hospital admissions and
647 upper respiratory viral loads. EBioMedicine. 2022;79:104008.
648 41. Paredes MI, Lunn SM, Famulare M, Frisbie LA, Painter I, Burstein R, et al. Associations Between
649 Severe Acute Respiratory Syndrome Coronavirus 2 (SARS-CoV-2) Variants and Risk of Coronavirus
650 Disease 2019 (COVID-19) Hospitalization Among Confirmed Cases in Washington State: A Retrospective
651 Cohort Study. Clin Infect Dis. 2022;75(1):e536-e44.
652 42. Van Goethem N, Chung PYJ, Meurisse M, Vandromme M, De Mot L, Brondeel R, et al. Clinical
653 Severity of SARS-CoV-2 Omicron Variant Compared with Delta among Hospitalized COVID-19 Patients in
654 Belgium during Autumn and Winter Season 2021–2022. Viruses. 2022;14(6):1297.
655 43. Beaudoin CA, Pandurangan AP, Kim SY, Hamaia SW, Huang CL, Blundell TL, et al. In silico analysis
656 of mutations near S1/S2 cleavage site in SARS-CoV-2 spike protein reveals increased propensity of
657 glycosylation in Omicron strain. J Med Virol. 2022;94(9):4181-92.
658 44. Morrison CB, Edwards CE, Shaffer KM, Araba KC, Wykoff JA, Williams DR, et al. SARS-CoV-2
659 infection of airway cells causes intense viral and cell shedding, two spreading mechanisms affected by IL-
660 13. Proceedings of the National Academy of Sciences. 2022;119(16):e2119680119.
661 45. Tran BM, Grimley SL, McAuley JL, Hachani A, Earnest L, Wong SL, et al. Air-Liquid-Interface
662 Differentiated Human Nose Epithelium: A Robust Primary Tissue Culture Model of SARS-CoV-2 Infection.
663 Int J Mol Sci. 2022;23(2).
664 46. Tan KS, Gamage AM, Liu J. Human Nasal Epithelial Cells (hNECs) Generated by Air-Liquid
665 Interface (ALI) Culture as a Model System for Studying the Pathogenesis of SARS-CoV-2. Methods Mol
666 Biol. 2022;2452:213-24.
667 47. Nori W, Ghani Zghair MA. Omicron targets upper airways in pediatrics, elderly and unvaccinated
668 population. World J Clin Cases. 2022;10(32):12062-5.
669 48. Armando F, Beythien G, Kaiser FK, Allnoch L, Heydemann L, Rosiak M, et al. SARS-CoV-2 Omicron
670 variant causes mild pathology in the upper and lower respiratory tract of hamsters. Nature
671 Communications. 2022;13(1):3519.
672 49. Karimizadeh Z, Dowran R, Mokhtari-Azad T, Shafiei-Jandaghi NZ. The reproduction rate of severe
673 acute respiratory syndrome coronavirus 2 different variants recently circulated in human: a narrative
674 review. Eur J Med Res. 2023;28(1):94.
675 50. St Hilaire BG, Durand NC, Mitra N, Pulido SG, Mahajan R, Blackburn A, et al. A rapid, low cost,
676 and highly sensitive SARS-CoV-2 diagnostic based on whole genome sequencing. bioRxiv.
677 2020:2020.04.25.061499.
678 51. Li Y, Renner DM, Comar CE, Whelan JN, Reyes HM, Cardenas-Diaz FL, et al. SARS-CoV-2 induces
679 double-stranded RNA-mediated innate immune responses in respiratory epithelial-derived cells and
680 cardiomyocytes. Proc Natl Acad Sci U S A. 2021;118(16).

681 52. Qiu Z, Hingley ST, Simmons G, Yu C, Das Sarma J, Bates P, et al. Endosomal proteolysis by
682 cathepsins is necessary for murine coronavirus mouse hepatitis virus type 2 spike-mediated entry. J
683 Virol. 2006;80(12):5768-76.
684 53. Lee RJ, Kofonow JM, Rosen PL, Siebert AP, Chen B, Doghramji L, et al. Bitter and sweet taste
685 receptors regulate human upper respiratory innate immunity. J Clin Invest. 2014;124(3):1393-405.
686 54. Sisson JH, Stoner JA, Ammons BA, Wyatt TA. All-digital image capture and whole-field analysis of
687 ciliary beat frequency. J Microsc. 2003;211(Pt 2):103-11.
688 55. Everett J, Hokama P, Roche AM, Reddy S, Hwang Y, Kessler L, et al. SARS-CoV-2 Genomic
689 Variation in Space and Time in Hospitalized Patients in Philadelphia. mBio. 2021;12(1):e03456-20.

690

691

Figures and Legends

Figure 1: Replication of SARS-CoV-2 WT (WA-1) and VOCs

(A&B) Human primary nasal epithelia ALI cultures (A) or Calu-3 cells (B) were infected with SARS-CoV-2 WT, Alpha, Beta, Delta and Omicron at MOI 0.1 PFU/cell and apically shed virus was titered by plaque assay at indicated hours post infection. (A) Titers from ALI are an average of 3 independent experiments including 9 individual donors per virus, each experiment was performed in triplicate. (B) Titers from Calu3 are an average of two independent experiments each in triplicates. (A and B) Graphed values represent mean with standard deviation, and statistics for both A and B were performed with ordinary two-way ANOVA comparing VOCs versus WT within a time point, multiple comparisons adjusted P-values: *P<0.01, **P<0.001, ***P<0.0001, ***P<0.00001.

Figure 2: Virus entry and spread.

(A) Calu3 cells were mock treated (DMSO), pre-infection treated with 20uM Nafamostat (Naf) for 2 hours, or pre- and post-infection treated with 20uM Naf for 2 hours. Infections with SARS-CoV-2 WT and VOCs were performed at MOI=0.1 and shed virus was collected at 16hpi for titer by plaque assay. (B) Percent inhibition in virus titer after Nafamostat treatments. (B and D) Graphed values represent mean with standard deviation, and statistics were performed with ordinary one-way ANOVA comparing the VOC against WT, adjusted P-values: *p<0.01, **p<0.001, ***p<0.0001, ****p<0.00001. (C) Protein lysates from ALI cells infected with SARS-CoV-2 WT and VOCs were analyzed by polyacrylamide gel electrophoresis followed by immunoblotting with antibodies against SARS-CoV-2 proteins, nucleocapsid (N) and spike which recognizes the full length (FL) and cleaved (S2) forms. Cellular protein GAPDH was used for loading control. (D) Percent cleaved spike was calculated as the fraction of cleaved spike (S2) over the sum of full length (FL) and cleaved (S2) spike, averaged from 3 independent

western blots. (E) A549^{ACE2} cells infected with SARS-CoV-2 WT and VOCs (MOI=0.01 for 24hpi), fixed and stained with fluorescently labeled antibodies DAPI (blue) and SARS-CoV-2 nucleocapsid (green). (F) Independent clusters expressing N were quantified for area (pixel^2) from 3 independent experiments. Graph represents individual values with mean in red, statistics were performed with two-way ANOVA with multiple comparisons of VOCs versus WT, adjusted P-values: **p<0.001, ***p<0.0001.

Figure 3: Comparison of plaque size and genome/PFU ratio among WT and VOC

(A) Plaque assay of SARS-CoV-2 viruses was performed on VeroE6^{TMPRSS2} cells. (B) Three independent plaque assays per virus were quantified for plaque area (pixel^2), and graph represents individual values with mean with standard deviation. Statistics were performed with ordinary two-way ANOVA comparing VOCs versus WT, adjusted P-values: **P<0.001, ***P<0.0001, ****P<0.00001. (C) The supernatant collected from Calu3 cells infected at MOI=0.1 at 24 hpi was measured for genomes using qRT-PCR with primers specific for SARS-CoV-2 RdRp and compared to PFUs measured by plaque assay. Values are an average of 3 independent experiments, each performed in triplicates. Graph represents mean with standard deviation, and statistics were performed with ordinary one-way ANOVA comparing VOCs versus WT, adjusted P-values: **P<0.001.

Figure 4: Comparison of interferon and interferon-induced responses to infections with SARS-CoV-2 VOCs

Infections with indicated viruses were performed in human A549^{ACE2} cells at MOI=2 for 48hpi (A), Calu3 cells at MOI=0.1 for 32hpi (B), and primary nasal epithelia ALIs infected at MOI=0.1 for 96hpi (C). At indicated time points RNA lysates were extracted for RT-qPCR with primers

specific to SARS-CoV-2 RdRp (i), human interferon-beta, IFNB (ii), interferon-lambda1, NFNL1 (iii), 2'-5'-oligoadenylate synthetase 2, OAS2 (iv) and interferon induced protein with tetratricopeptide repeats 1, IFIT1 (v). Black bars indicate WT virus, red for Alpha, blue for Beta, green for Delta and orange for Omicron. For each cell type, graphs represent one of two independent experiments, each performed in biological triplicates. Graphed values are mean with standard deviation, and statistics were performed with ordinary one-way ANOVA comparing VOCs versus WT, adjusted P-values: *P<0.01, **P<0.001, ***P<0.0001, ***P<0.00001.

Figure 5: dsRNA-activated pathways with SARS-CoV-2 infections.
(A) Primary nasal cells were infected at MOI=0.1. Protein lysate was collected at 96hpi and analyzed by immunoblot for phosphorylated PRK (p-PKR), PKR, phosphorylated eIF2α (p-eIF2 α), eIF2 α, SARS-CoV-2 nucleocapsid (N) and GAPDH. (B) A549^{ACE2} cells were infected with SARS-CoV-2 viruses at MOI=0.1 for 72hpi. Protein lysates were analyzed by immunoblot for p-PKR, PKR, p-eIF2α, eIF2α, N and GAPDH. (C) Infections with SARS-CoV-2 viruses were performed in A549^{ACE2} at MOI=0.1 for 48hpi, and 24hpi for SINV. RNA lysates were analyzed on a Bioanalyzer, arrows indicate bands of degraded RNAs.

Figure 6: SARS-CoV-2 VOC infections damage primary nasal cultures
Primary nasal epithelia were infected with SARS-CoV-2 viruses at MOI=0.1 and processed at 96hpi for various assays. (A) Transepithelial electrical resistance (TEER) was measured post SARS-CoV-2 infection of nasal ALI cultures at 0, 48 and 96hpi. Values represent the difference in TEER (ΔTEER) during the indicated time span, from an average from 3 independent experiments. Graphed values are mean with standard deviation, and statistics were performed

with ordinary two-way ANOVA comparing VOCs versus WT within a time span, multiple comparison adjusted P-values: *P<0.01. (B) Ciliary beat frequency was measured in live ALI cultures post SARS-CoV-2 infection. (C and D) Infected and uninfected (mock) cultures from separate donors were fixed at 96hpi for immunofluorescence and confocal imaging. Antibodies were used to label DAPI (blue), Tub4b (green) and SARS-CoV-2 nucleocapsid (red). Arrows indicate syncytia-like clusters. Scale bars indicate 50um (C) and 10um (D). Images are representative of infections in multiple donors. (E) Real-time videos of infected and mock ALIs at 9hpi were quantified for the area of actively beating cilia. (B and E) Graphed values represent mean with standard deviation and statistics were performed with one-way ANOVA using Dunnett's multiple comparisons test for all infected conditions against mock/uninfected, with adjusted P-values: *P<0.05, **P<0.005, ****P<0.00005.

Figure 7: Delaware Valley SARS-CoV-2 surveillance data

(A) Effect size of variants on clinical qPCR assay Ct (compared to pre-VOC), adjusted for time during wave, specimen type, and qPCR machine as captured using a Bayesian regression model. The X-axis shows the marginal effect on Ct for each variant compared to preVOC. Note that a 1 cycle change in Ct is roughly equivalent to a 2-fold increase in RNA abundance under ideal PCR conditions. The Y-axis shows the posterior probability density generated from the Bayesian regression model.

Supplemental Figure 1: SARS-CoV-2 infections in cell lines.

(S1A) SARS-CoV-2 stocks were harvested from VeroE6^{TMPRSS2} cell line after 2 passages followed by RNA collection and sequencing for substitutions. The virus sequence was aligned against the Washinton-A strain for reference. A mutation is indicated with a colored circle, black

for WT, red for Alpha, blue for Beta, green for Delta and orange for Omicron. The fraction of sequences with indicated mutation is denoted as pie slice within the circle.

Supplemental Figure 2: SARS-CoV-2 infections in lower respiratory cell lines

(A) VeroE6^{TMPRSS2} cells were infected with SARS-CoV-2 viruses and protein lysates were collected at 48 hpi for western. The membrane was blotted for SARS-CoV-2 nucleocapsid (N) and spike protein (S2). Percent of cleaved spike was calculated as the fraction of cleaved spike (S2) over the sum of full length (FL) and cleaved (S2) spike, averaged from 3 independent western blots. (B) Calu3 cells were infected with SARS-CoV-2 viruses at MOI=0.1 and RNA was collected at 24 hpi. RT-qPCR was performed with primers specific for SARS-CoV-2 RdRp to quantify virus genomes. (C) A549^{ACE2} cells were infected with SARS-CoV-2 viruses at MOI=0.1 and supernatant was collected at indicated timepoints for titer virus by plaque assay. Graphed values represent mean with standard deviation, and statistics were performed with ordinary two-way ANOVA with multiple comparisons for VOCs versus WT within a time point, adjusted P-values: *P<0.05, **P<0.005, ***P<0.0005.

Supplemental Figure 3: SARS-CoV-2 infections in nasal ALIs

(A) Nasal ALI cultures composed of 4 donor cells pooled together were infected simultaneously at 33°C and 37°C with SARS-CoV-2 WT, Delta and Omicron viruses at MOI 0.1. Apically shed virus was collected at indicated time points for titer by plaque assay. Growth curves at 33°C are indicated with dashed lines, and 37°C with solid lines. Graphed values represent mean with standard deviation and statistics were performed with ordinary two-way ANOVA with multiple comparisons for VOCs versus WT within a time point. Values did not reach statistical significance. (B) ALI cells were infected at MOI=0.1; at 96 hpi sample was fixed and processed

by immunofluorescence for DAPI (blue), Tub4 (green) and SARS-CoV-2 nucleocapsid (red). (C) Infected and mock cultures (also depicted in Fig 6D) were fixed for immunofluorescence and confocal imaging. Antibodies were used to label SARS-CoV-2 nucleocapsid (red) and phalloidin (white). Arrow indicates syncytia-like clusters. Images are representative of infections in multiple donor ALI cultures.

Fig1

A

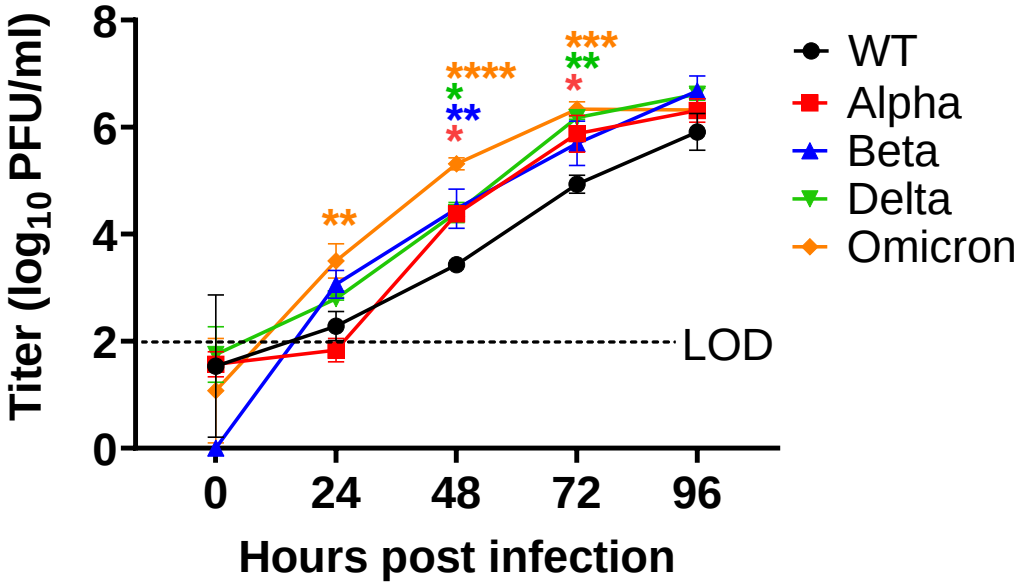
Titer (log10 PFU/ml)
8
6
4
2
0
0
24
48
72
96
Hours post infection
LOD
WT
Alpha
Beta
Delta
Omicron
**
****
*
**
*
***
**
*

B

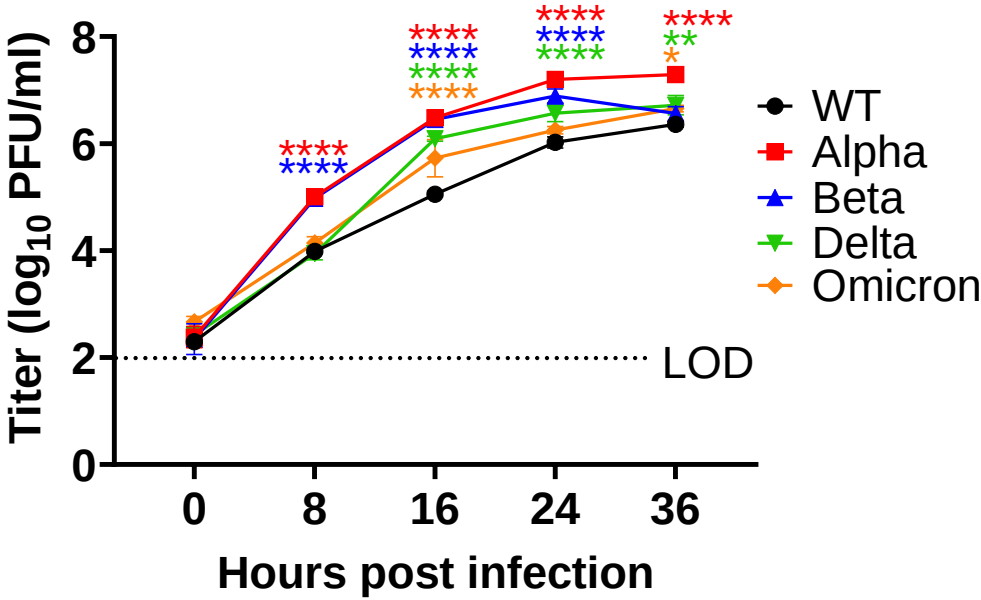
Titer (log10 PFU/ml)
8
6
4
2
0
0
8
16
24
36
Hours post infection
LOD
WT
Alpha
Beta
Delta
Omicron
****
****
****
****
****
****
****
****
****
**
*

Fig 2

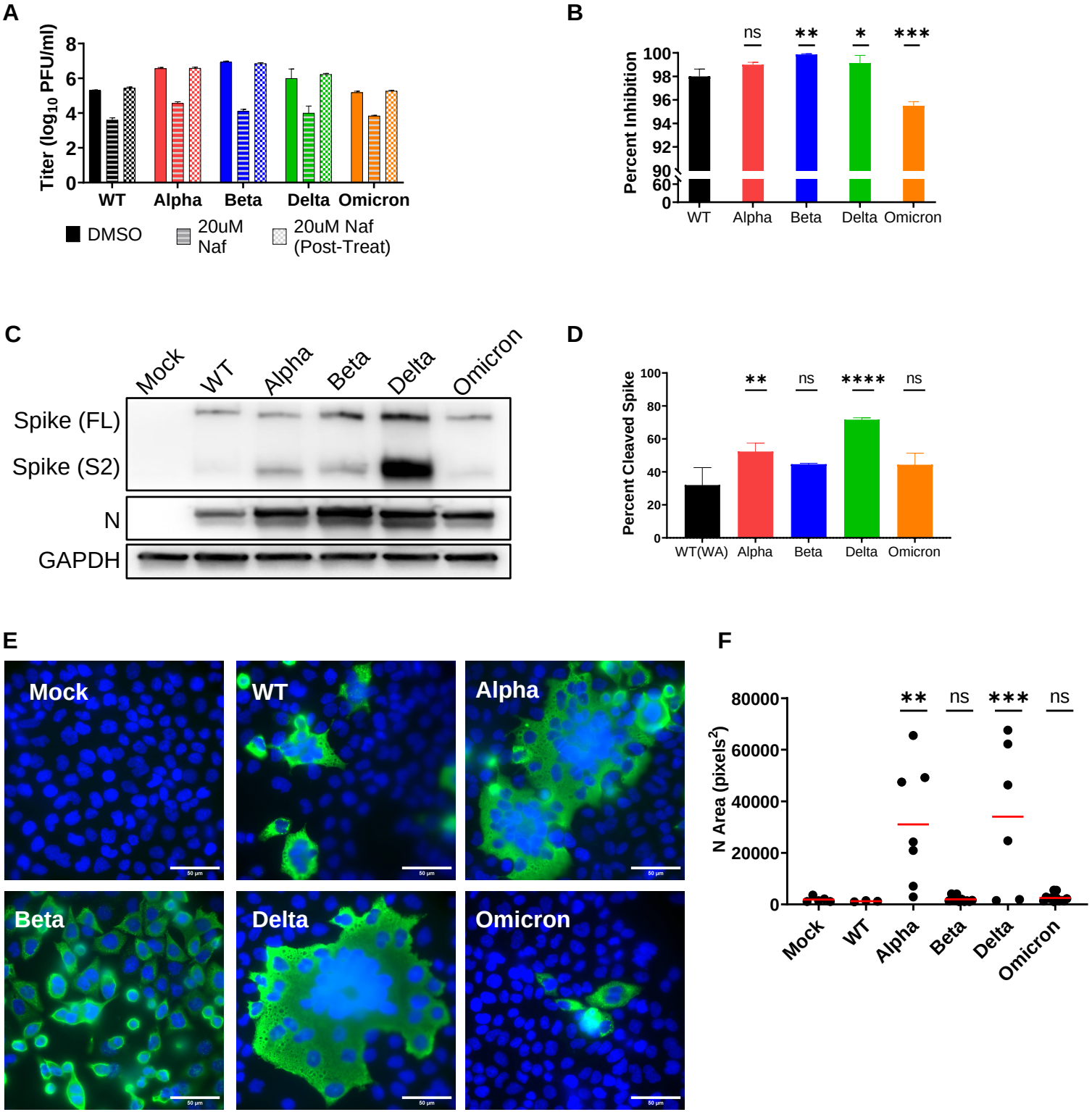
A
Titer (log10 PFU/ml)
8
6
4
2
0
WT
Alpha
Beta
Delta
Omicron
DMSO
20uM Naf
20uM Naf (Post-Treat)
B
Percent Inhibition
100
98
96
94
92
90
60
0
ns
**
*
***
WT
Alpha
Beta
Delta
Omicron
C
Mock
WT
Alpha
Beta
Delta
Omicron
Spike (FL)
Spike (S2)
N
GAPDH
D
Percent Cleaved Spike
100
80
60
40
20
0
**
ns
****
ns
WT(WA)
Alpha
Beta
Delta
Omicron
E
Mock
WT
Alpha
Beta
Delta
Omicron
F
N Area (pixels2)
80000
60000
40000
20000
0
**
ns
***
ns
Mock
WT
Alpha
Beta
Delta
Omicron

Fig3

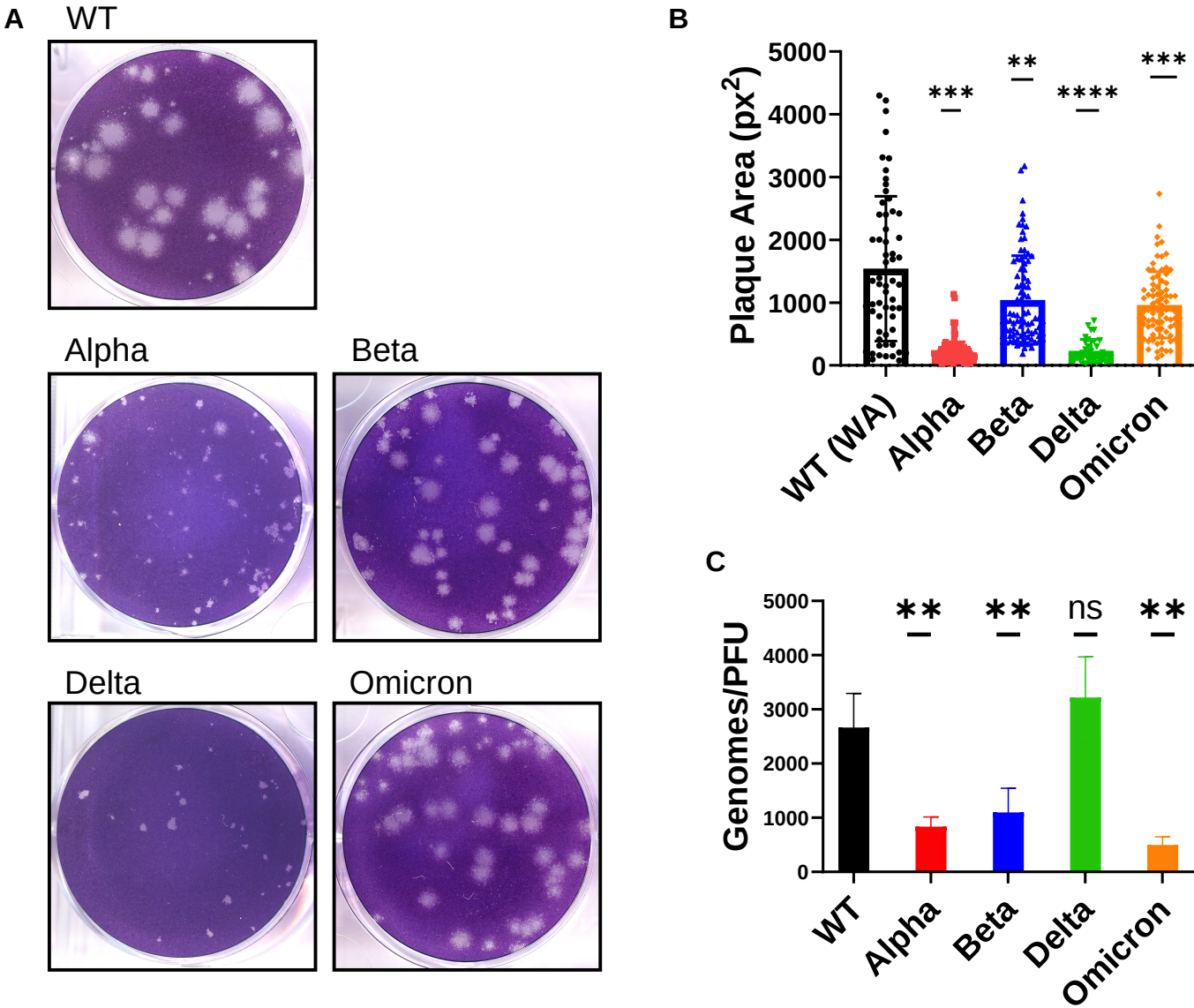
A
WT
Alpha
Beta
Delta
Omicron
B
Plaque Area (px2)
5000
4000
3000
2000
1000
0
***
**
****
***
WT (WA)
Alpha
Beta
Delta
Omicron
C
Genomes/PFU
5000
4000
3000
2000
1000
0
**
**
ns
**
WT
Alpha
Beta
Delta
Omicron

Fig 4

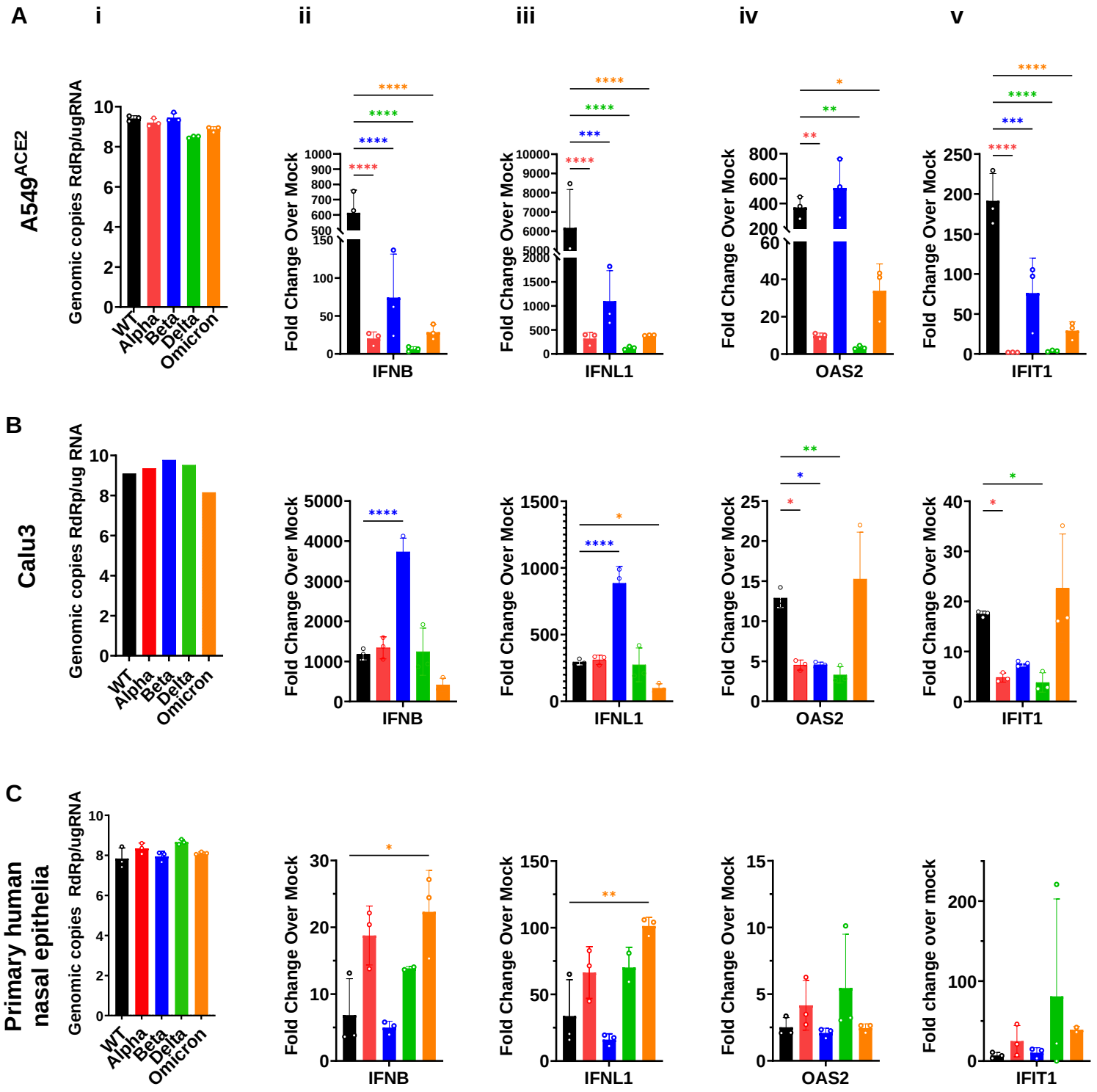
A
i
ii
iii
iv
v
A549ACE2
Genomic copies RdRp/ugRNA
Fold Change Over Mock
IFNB
IFNL1
OAS2
IFIT1
WT
Alpha
Beta
Delta
Omicron
B
Calu3
Genomic copies RdRp/ug RNA
C
Primary human nasal epithelia
Genomic copies RdRp/ugRNA
Fold change over mock

Fig 5

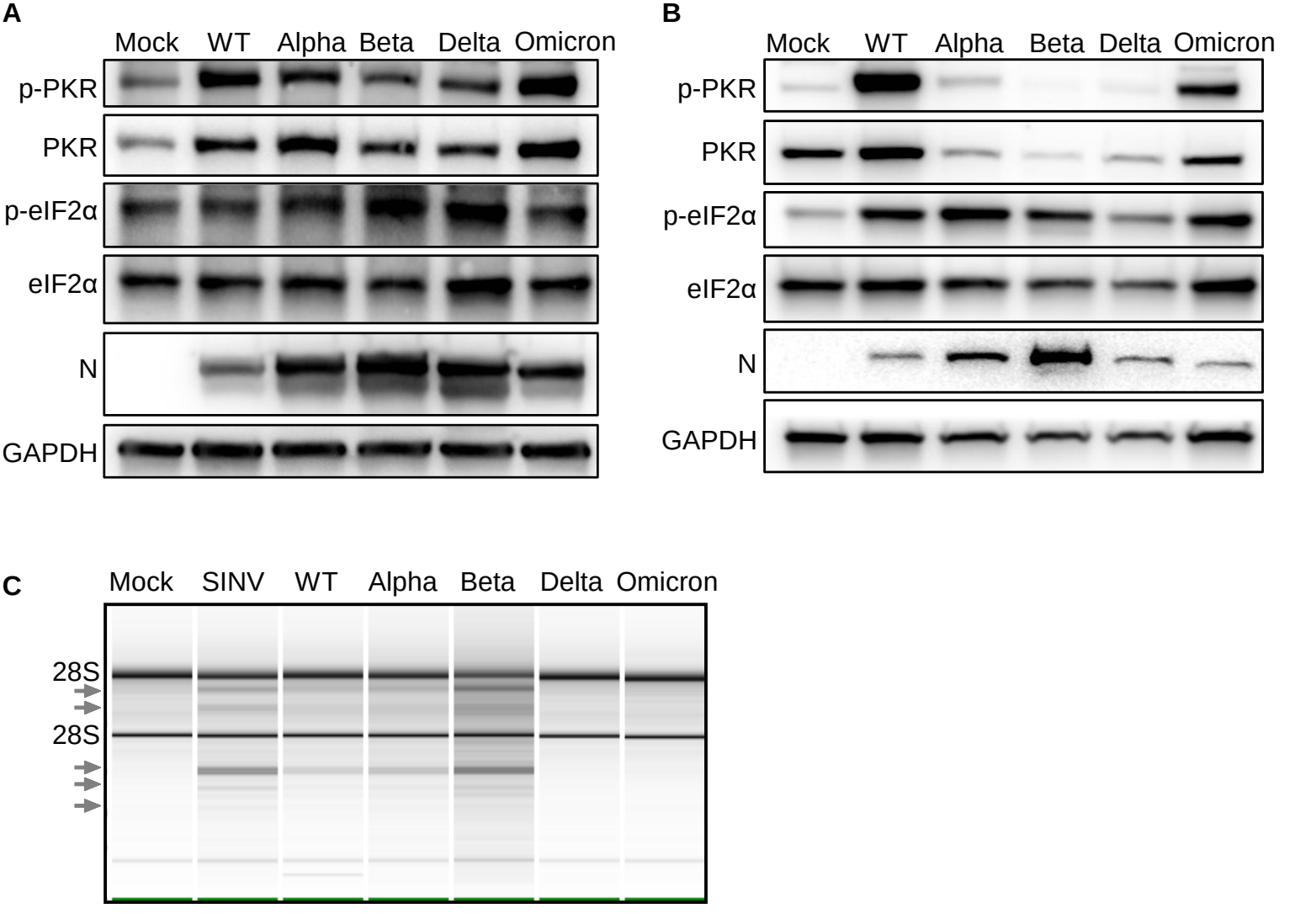
A
Mock
WT
Alpha
Beta
Delta
Omicron
p-PKR
PKR
p-eIF2α
eIF2α
N
GAPDH
B
Mock
WT
Alpha
Beta
Delta
Omicron
p-PKR
PKR
p-eIF2α
eIF2α
N
GAPDH
C
Mock
SINV
WT
Alpha
Beta
Delta
Omicron
28S
28S

Fig 6

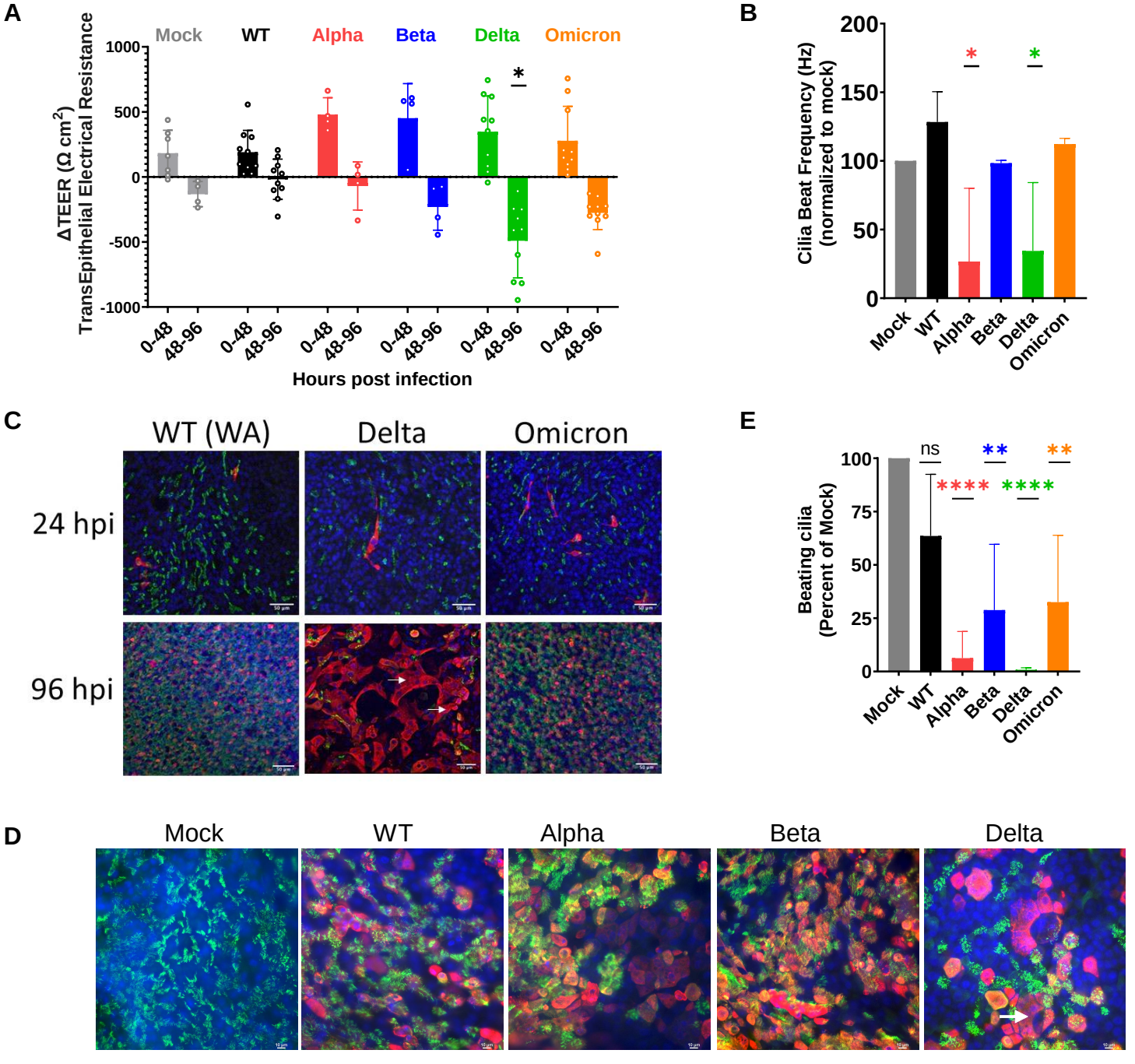
A
Mock
WT
Alpha
Beta
Delta
Omicron
ΔTEER (Ω cm²)
TransEpithelial Electrical Resistance
1000
500
0
-500
-1000
*
0-48
48-96
Hours post infection
B
Cilia Beat Frequency (Hz)
(normalized to mock)
200
150
100
50
0
*
*
Mock
WT
Alpha
Beta
Delta
Omicron
C
WT (WA)
Delta
Omicron
24 hpi
96 hpi
E
Beating cilia
(Percent of Mock)
100
75
50
25
0
ns
**
**
****
****
Mock
WT
Alpha
Beta
Delta
Omicron
D
Mock
WT
Alpha
Beta
Delta

Fig 7

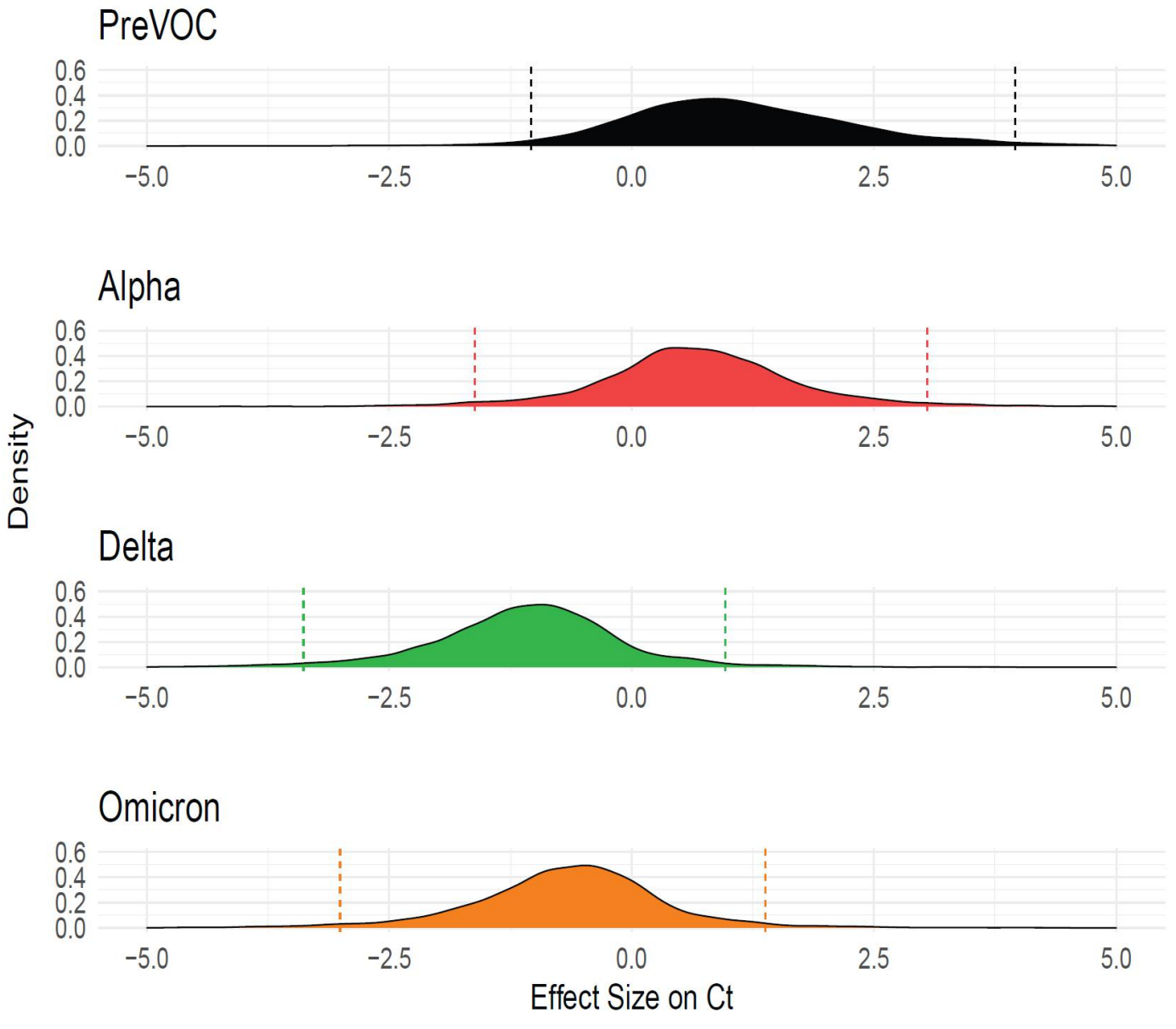
PreVOC
Alpha
Delta
Omicron
Density
0.6
0.4
0.2
0.0
−5.0
−2.5
0.0
2.5
5.0
Effect Size on Ct

Fig S1: Genome alignment

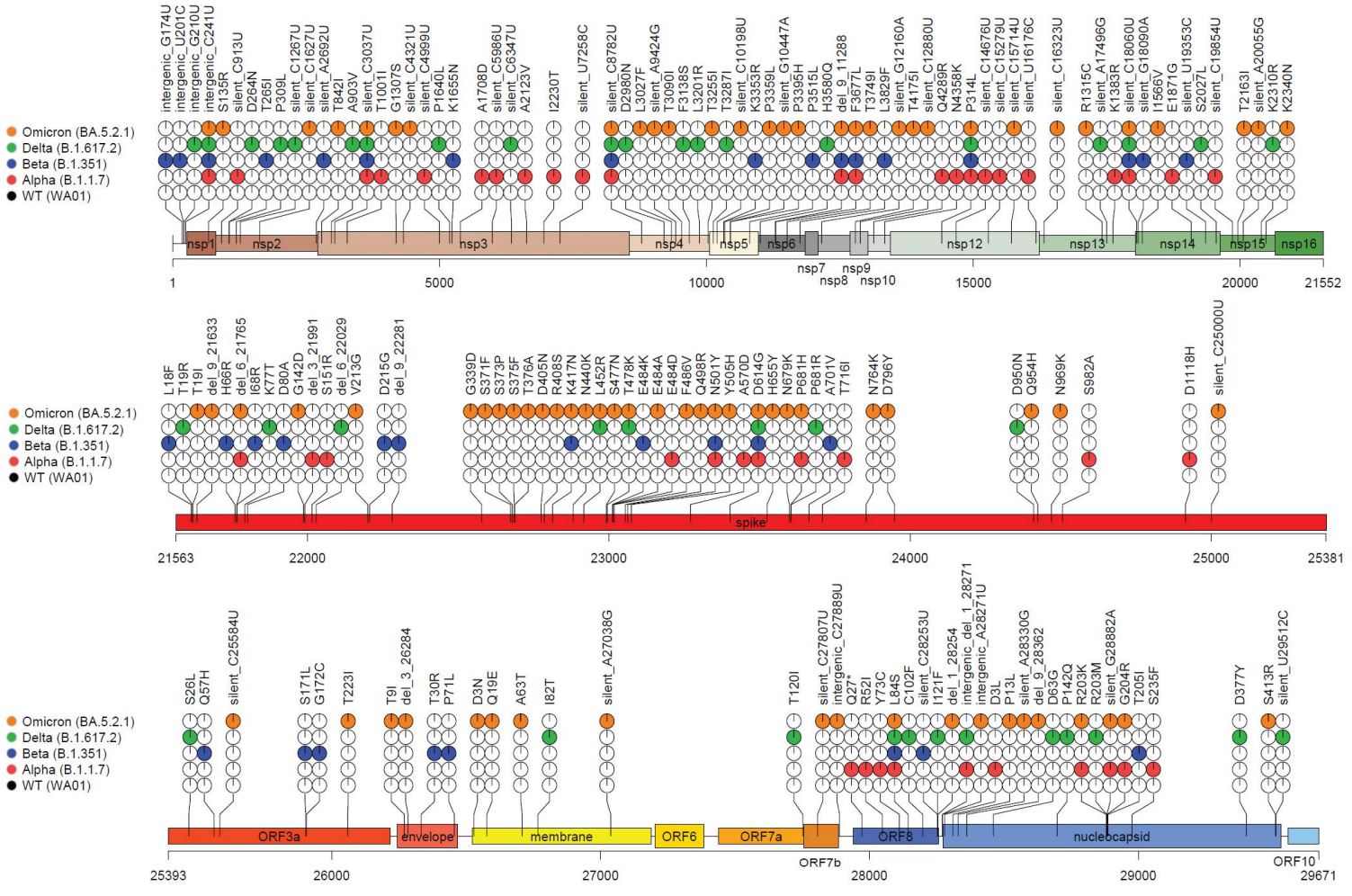

Fig S2

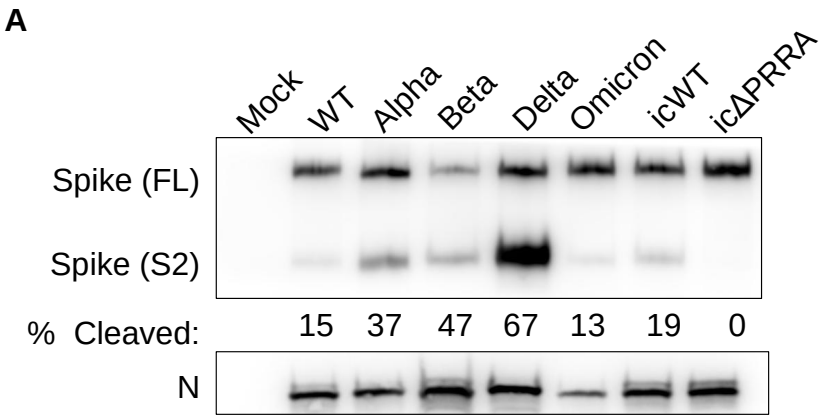
A
Mock
WT
Alpha
Beta
Delta
Omicron
icWT
icΔPRRA
Spike (FL)
Spike (S2)
% Cleaved:
15
37
47
67
13
19
0
N

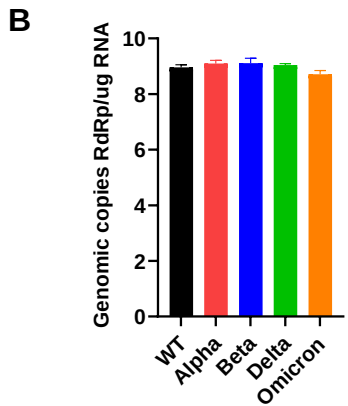
B
Genomic copies RdRp/ug RNA
10
8
6
4
2
0
WT
Alpha
Beta
Delta
Omicron

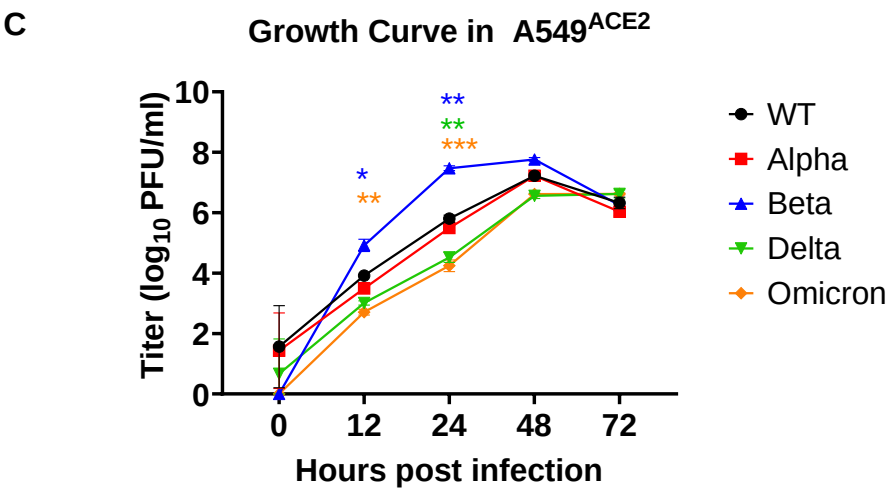
C
Growth Curve in A549ACE2
Titer (log10 PFU/ml)
10
8
6
4
2
0
0
12
24
48
72
Hours post infection
*
**
**
**
***
WT
Alpha
Beta
Delta
Omicron

Fig S3

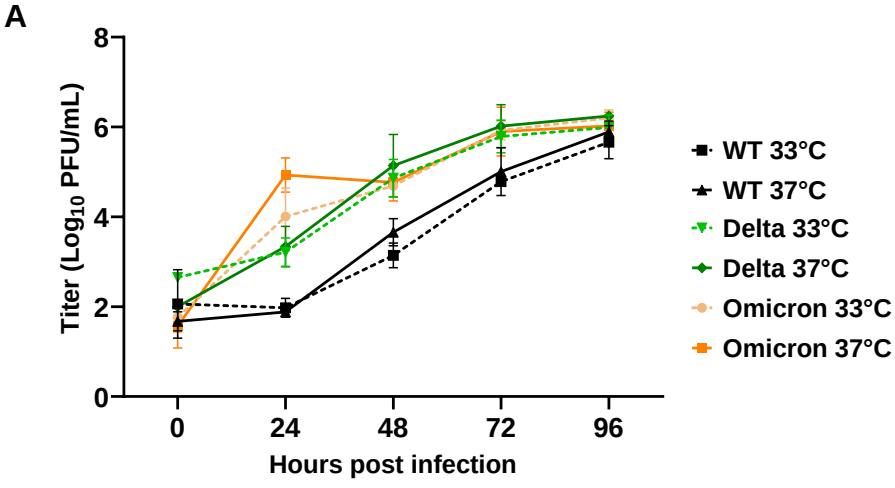
A
Titer (Log10 PFU/mL)
8
6
4
2
0
0
24
48
72
96
Hours post infection
WT 33°C
WT 37°C
Delta 33°C
Delta 37°C
Omicron 33°C
Omicron 37°C

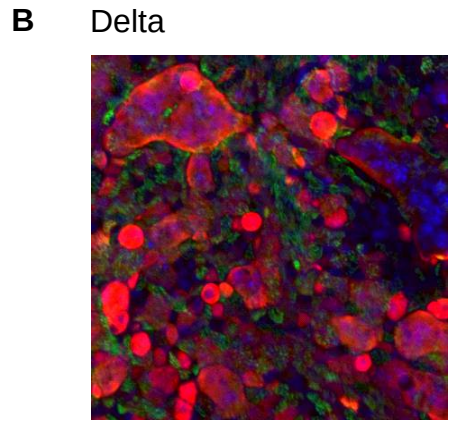
B
Delta

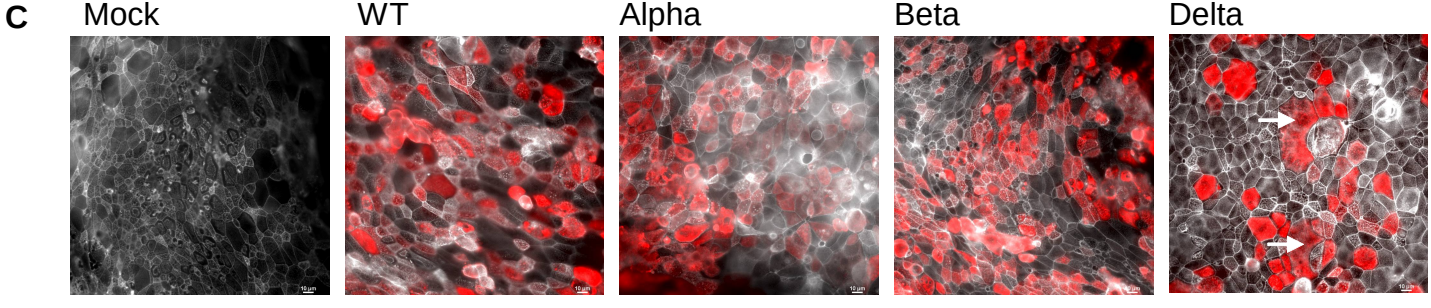
C
Mock
WT
Alpha
Beta
Delta